Biomedical Photonics HANDBOOK

Editor-in-Chief
Tuan Vo-Dinh

CRC PRESS

Boca Raton London New York Washington, D.C.

Cover Art: *Field of Lights*, oil painting by Kim-Chi Le Vo-Dinh. Reproduced with permission of the artist.

Library of Congress Cataloging-in-Publication Data

Biomedical photonics handbook / edited by Tuan Vo-Dinh.
p. cm.
Includes bibliographical references and index.
ISBN 0-8493-1116-0
1. Optoelectronic devices—Handbooks, manuals, etc. 2. Biosensors—Handbooks, manuals, etc. 3. Diagnositic imaging—Handbooks, manuals, etc. 4. Imaging systems in medicine—Handbooks, manuals, etc. I. Vo-Dinh, Tuan.

R857.06 B573 2002
610′.28—dc21 2002034914

Visit the CRC Press Web site at www.crcpress.com

International Standard Book Number 0-8493-1116-0
Library of Congress Card Number 2002034914
Printed in the United States of America 1 2 3 4 5 6 7 8 9 0
Printed on acid-free paper

21

Functional Imaging with Diffusing Light

Arjun G. Yodh
University of Pennsylvania
Philadelphia, Pennsylvania

David A. Boas
Harvard Medical School
Massachusetts General Hospital
Athinoula A. Martinos Center for Biomedical Imaging
Charlestown, Massachusetts

21.1 Introduction

Many materials are visually opaque because photons traveling within them are predominantly scattered rather than absorbed. Some common examples of these highly scattering media include white paint, foam, mayonnaise, and human tissue. Indeed, anyone who has held a flashlight up to his or her hand will notice some of this light is transmitted, albeit after experiencing many scattering events. Light travels through these materials in a process similar to heat diffusion.

What does it mean to say light transport is diffusive? Consider a simple experiment in which an optical fiber is used to inject light into a highly scattering material such as paint or tissue. Microscopically, the injected photons experience thousands of elastic scattering events in the media. A few of the photons will be absorbed by chromophores and will be lost. The remaining photons travel along pathways that resemble a random walk. These individual trajectories are composed of straight-line segments with sudden interruptions where the photon propagation direction is randomly changed. The average length of the straight-line segments is called the random walk steplength of the traveling photon. By summing all trajectories one can compute the photon concentration or photon fluence rate as a function of time and position within the media.

It is then straightforward to show that the collective migration of photon concentration is described by a diffusion equation. In practice one can carry out a variety of measurements to confirm the diffusive

0-8493-1116-0/03/$0.00+$1.50

nature of light transport. For example, if a short pulse of light is injected into the medium and a second optical fiber is used to detect transmitted photons, then, when the transport is diffusive, the most probable arrival times for the detected photons will scale with the square of the source-detector separation divided by the random walk steplength.

Diffuse light imaging and spectroscopy aims to investigate tissue physiology millimeters to centimeters below the tissue surface.[1–5] The cost of this goal is that we must abandon traditional optical spectroscopies and traditional microscopy because traditional methodologies require optically thin samples. In addition, light penetration must be large in order to reach tissue located centimeters below the surface. Fortunately, a spectral window exists within tissues in the near-infrared from 700 to 900 nm, wherein photon transport is dominated by scattering rather than absorption. The absorption of hemoglobin and water is small in the near-infrared, but elastic scattering from organelles and other microscopic interfaces is large. These are precisely the conditions required for application of the diffusion model. The recognition and widespread acceptance that light transport over long distances in tissues is well approximated as a diffusive process has propelled the field. Using this physical model it is possible to separate tissue scattering from tissue absorption quantitatively, and to incorporate the influence of boundaries, such as the air-tissue interface, into the transport theory accurately. The diffusion approximation also provides a tractable basis for tomographic approaches to image reconstruction using highly scattered light. Tomographic methods were not employed in early transillumination patient studies, and are crucial for recovery of information about tissue optical property heterogeneity.

Even though absorption in the near-infrared is relatively small, the spectra of major tissue chromophores, particularly oxy- and deoxyhemoglobin and water, differ significantly in the near-infrared. As a result, the diffuse optical methods are sensitive to blood dynamics, blood volume, blood oxygen saturation, and water and lipid content of interrogated tissues. In addition, one can induce optical contrast in tissues with exogenous contrast agents, for example, chemical species that occupy vascular and extravascular space and preferentially accumulate in diseased tissue. Together these sensitivities provide experimenters with access to a wide spectrum of biophysical problems. The greater blood supply and metabolism of tumors compared to surrounding tissues provides target heterogeneity for tissue maps based on absorption.[6–25] Similar maps can be applied for studies of brain bleeding[26–28] and cerebral oxygen dynamics associated with activation by mental and physical stimulation.[29–41] Other applications of the deep tissue methods include the study of mitochondrial diseases,[42–44] of muscle function and physiology,[45,46] and of photodynamic therapy.[47–51]

Biomedical applications for diffusing near-infrared light probes parallel the application of nuclear magnetic resonance to tissue study. Generally, the categories of measurement can be termed spectroscopy and imaging. Spectroscopy is useful for measurement of time-dependent variations in the absorption and scattering of large tissue volumes. For example, brain oximetry (hemoglobin spectroscopy) of the frontal, parietal, or occipital regions can reveal reduced brain perfusion caused by head injury. Imaging is important when a localized heterogeneity of tissue is involved, for example, an early breast or brain tumor, a small amount of bleeding in the brain, or an early aneurysm. Images enable one to identify the site of the trauma and differentiate it from background tissue. Imaging is also important because it improves the accuracy of a spectroscopic measurement. Typically, spectroscopic methods employ oversimplified assumptions about the scattering media. Imaging relaxes some of these assumptions, usually at the cost of a more complex experimental instrument and computation, and ultimately improves the fidelity of the gathered optical property information.

The purpose of this chapter is to discuss functional imaging with diffusing photons. Our emphasis will be on imaging rather than spectroscopy, but it will be necessary to briefly review the basics of diffuse optical spectroscopy. This chapter is intended as a tutorial about what can be done with diffuse optical imaging, how to do it, and how to understand it. We intend to give a tutorial snapshot of the field with selected examples, but not a comprehensive review of research in the field. The remainder of this tutorial consists of sections on theory, instrumentation, and imaging examples, and a discussion about limitations and compromises associated with the technique.

21.2 Theory

21.2.1 Diffusion Approximation

Many researchers (e.g., References 52 through 56 and others) have shown that the photon fluence rate, $\Phi(r, t)$ (photons/[cm^2 · s]), obeys the following diffusion equation in highly scattering media:

$$\nabla \cdot D(\mathbf{r})\nabla\Phi(\mathbf{r},t) - v\mu_a(\mathbf{r})\Phi(\mathbf{r},t) + vS(\mathbf{r},t) = \frac{\partial\Phi(\mathbf{r},t)}{\partial t}. \qquad (21.1)$$

$\Phi(r,t)$ is proportional to the photon number density $U(r, t)$ (photons/cm^3), i.e., $\Phi(r, t) = vU(r, t)$. The turbid medium is characterized by a speed of light, v, an absorption coefficient μ_a (i.e., the multiplicative inverse of the photon absorption length), and a photon diffusion coefficient, $D = v/3(\mu_s' + \mu_a) \equiv v/3(\mu_s')$; the dependence of D on μ_a is a subject of recent debate,[53, 57–68] but the latter relation follows in most tissues wherein $\mu_s' >> \mu_a$. The medium's reduced scattering coefficient is defined as $\mu_s' = (1 - g)\mu_s$ and represents the multiplicative inverse of the photon random walk steplength, l^*. Here μ_s is the reciprocal of the photon scattering length, l, and $g = \langle\cos\theta\rangle$ is the ensemble-averaged cosine of the scattering angle θ associated with a typical single scattering event in the sample; g accounts for the fact that light is more typically scattered in the forward direction, so that many scattering events are required before the initial photon propagation direction is truly randomized. $S(r, t)$ is an isotropic source term that gives the number of photons emitted at position r and time t per unit volume per unit time.

The right-hand side of Equation 21.1 represents the rate of increase of photons within a sample volume element. This rate equals the number of photons scattered into the volume element per unit time from its surroundings, *minus* the number of photons absorbed per unit time within the volume element, *plus* the number of photons emitted per unit time from any sources in the volume element.

The diffusion equation is based upon the $P1$ approximation of the linear transport equation.[69,70] It is valid when the reduced albedo $\alpha' = \mu_s'/(\mu_a + \mu_s')$ is close to unity, i.e., the reduced scattering coefficient is much greater than the absorption coefficient ($\mu_s' >> \mu_a$). The near-infrared (NIR) spectral window (commonly called the "therapeutic" window) of biological tissue lies between the intense visible absorption bands of hemoglobin and the NIR absorption band of water. In this window the reduced scattering coefficient is often 10 to 1000 times greater than the absorption coefficient,[71] for example, $\mu_s' = 10$ cm^{-1} and $\mu_a = 0.03$ cm^{-1} at 800 nm in human breast tissues. Of course tissues are not homogeneous, but they can be accurately divided into domains of piecewise homogeneous turbid media, each obeying Equation 21.1. Measurements are accomplished using sources and detectors arranged on the surfaces of or embedded within the tissue. Strictly speaking, it is also important for the source-detector separation to be of order three photon random walk steps (i.e., $3l^*$) or larger; otherwise the photon scattering angles will not be sufficiently randomized at the point of detection for rigorous application of the diffusion approximation.[72,73]

21.2.2 Sources of Diffusing Photons

Three types of sources are commonly employed in diffusive light measurements (see Figure 21.1). The simplest and easiest method to use is the continuous-wave (CW) device. In this case the source amplitude is constant, and the transmitted amplitude is measured as a function of source-detector separation or wavelength. The second method is the pulsed-time or time-resolved technique. In this scheme a short, usually subnanosecond light pulse is launched into the medium, and the temporal point spread function of the transmitted pulse is measured. The third method is the intensity modulated or frequency-domain technique. In this case the amplitude of the input source is sinusoidally modulated, producing a diffusive wave within the medium. The amplitude and phase of the transmitted diffuse light wave are then measured. These methods are related; the time-resolved and frequency-domain approaches are Fourier

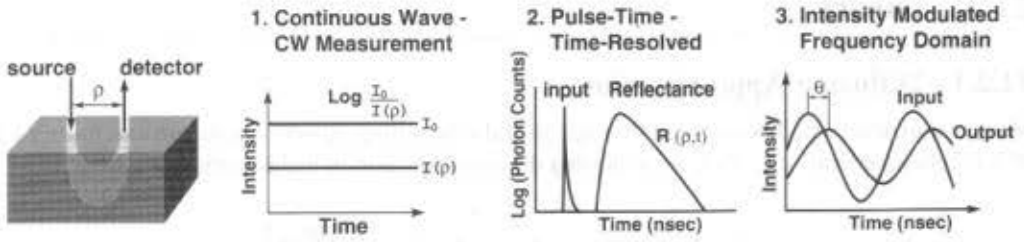

FIGURE 21.1 Three source-detector schemes are generally employed in the photon migration field. On the far left we illustrate a typical remission geometry: (1) continuous-wave, called CW spectroscopy; (2) time-pulsed or time-resolved technique (often called TRS); (3) intensity amplitude modulation, i.e., often referred to as the frequency-domain method.

transformations of one another, and the CW approach is a special case of the frequency-domain approach wherein the modulation frequency is zero. Each of these approaches has strengths and weaknesses.

Briefly, the CW scheme is inexpensive and provides for rapid data collection. However, because it measures amplitude only, it lacks the capability for characterizing simultaneously the absorption and scattering of even a homogeneous medium from a measurement using only a single source-detector pair. The more expensive time-resolved scheme collects the full temporal point spread function, which is equivalent to a frequency domain measurement over a wide range of modulation frequencies. In this case, when the medium is homogeneous, μ_a and μ_s' can be obtained simultaneously from a single source-detector separation. The photon counting, however, can be slow and the technique is often limited by shot noise. The frequency domain technique is a compromise between CW and time-resolved techniques, with respect to cost and speed. It concentrates all the light energy into a single modulation frequency. It measures amplitude and phase, which ideally enable us to obtain μ_a and μ_s' for a homogeneous medium using a single source-detector separation. In practice all of these methods benefit significantly from use of many source-detector pairs and many optical wavelengths. In this chapter we focus on frequency domain sources, but the results can be applied to time-resolved and CW methods.

21.2.3 Diffuse Photon Density Waves in Homogeneous Turbid Media

Consider a light source at the origin with its intensity sinusoidally modulated at a modulation frequency f, e.g., the source term in Equation 21.1 is $S(\mathbf{r},t) = (M_{dc} + M_{ac}e^{-i\omega t})\,\delta(\mathbf{r})$, where $\omega = 2\pi f$ is the angular source modulation frequency, M_{dc} and M_{ac} are the source strengths of the DC and AC source components. The diffusion equation continues to be valid for light derived from these highly modulated sources as long as the modulation frequency ω is significantly smaller than the scattering frequency $v\mu_s'$; that is, photons must experience many scattering events during a single modulation period. Photons leaving the source and traveling along different random walk trajectories within the turbid medium will add incoherently to form a macroscopic scalar wave of photon concentration or fluence rate.

The total fluence rate consists of a DC and an AC component, i.e., $\Phi_{total}(\mathbf{r},t) = \Phi_{DC}(\mathbf{r}) + \Phi_{AC}(\mathbf{r}, t)$. We focus on the AC component $\Phi_{AC}(\mathbf{r},t) = \Phi(\mathbf{r})e^{-i\omega t}$. The photon fluence will oscillate at the source of modulation frequency ω. Plugging the AC source term into Equation 21.1 we obtain the following Helmholtz equation for the oscillating part of the photon fluence:

$$\left(\nabla^2 + k^2\right)\Phi(\mathbf{r}) = -\left(\frac{vM_{ac}}{D}\right)\delta(\mathbf{r}). \tag{21.2}$$

We refer to this disturbance as a diffuse photon density wave (DPDW).[74,75] The DPDW has wavelike properties; for example, refractive,[76] diffractive,[77] and dispersive[78] behaviors of the DPDW have been demonstrated.

The photon density wave has a simple spherical wave solution for an infinite homogeneous highly scattering medium of the form:

$$\Phi_{AC}(\mathrm{r},t)=\left(\frac{vM_{ac}}{4\pi Dr}\right)\exp(ikr)\exp(-i\omega t). \tag{21.3}$$

The diffuse photon density wave wavenumber is complex, $k = k_r + ik_i$, and $k^2 = (-v\mu_a + i\omega)/D$. The real and imaginary parts of the wavenumber are:

$$k_r=\left(\frac{v\mu_a}{2D}\right)^{1/2}\left(\left(1+\left(\frac{\omega^2}{v\mu_a}\right)\right)^{1/2}-1\right)^{1/2}$$
$$k_i=\left(\frac{v\mu_a}{2D}\right)^{1/2}\left(\left(1+\left(\frac{\omega^2}{v\mu_a}\right)\right)^{1/2}+1\right)^{1/2}. \tag{21.4}$$

In Figure 21.2 the measured wave is demonstrated within a tank of homogeneous highly scattering Intralipid. Constant-phase contours are shown in 20° intervals about the source at the origin. We see that the wave contours are circular and that their radii can be extrapolated back to the source. In the inset we exhibit the phase shift and a simple function of the wave amplitude plotted vs. the source-detector separation. From the slopes of these linear position-dependent measurements, one can deduce the wavelength of the disturbance, as well as the absorption and scattering factors of the homogeneous turbid medium via Equations 21.3 and 21.4.

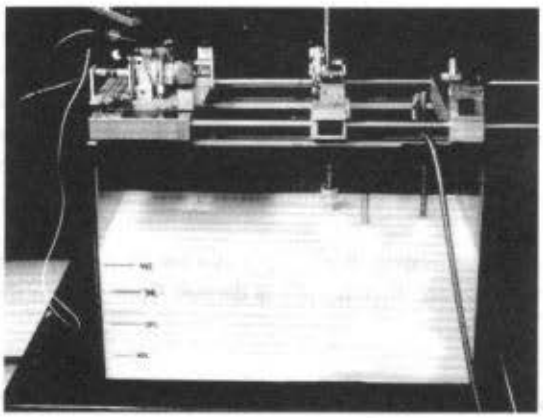

A

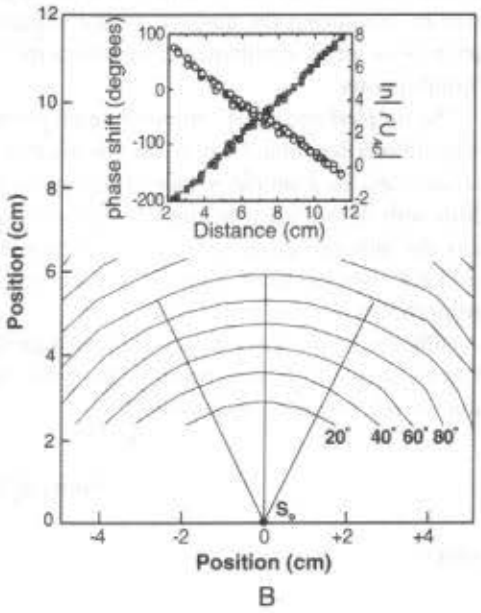

B

FIGURE 21.2 (A) An aquarium used for model experiments. The aquarium is filled with Intralipid, a polydisperse emulsion whose absorption and scattering coefficients in the NIR region can be adjusted to approximate those of tissue. (B) Constant-phase contours of diffuse photon-density waves in the homogeneous sample of Intralipid. The source for this measurement is a 1-mW laser diode operating at 780 nm and modulated at 200 MHz. Inset: Measured phase-shift and a dimensionless (logarithmic) function of the amplitude as a function of source-detector separation.

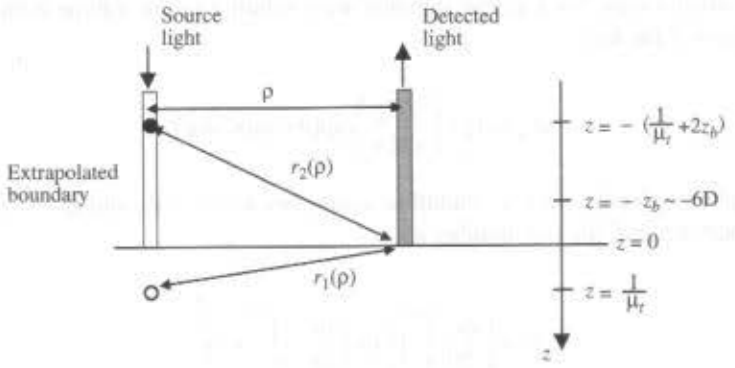

FIGURE 21.3 Schematic of the experimental fiber configuration showing the relative positions of surface boundary ($z = 0$), extrapolated boundaries, $r_1(\rho)$ and $r_2(\rho)$ as defined in Equations 21.5, 21.6a, and 21.6b.

For homogeneous media in more complex geometries, one can still derive a set of phase and amplitude curves as a function of source-detector separation. The functional relationships may not be linear, but it is still readily possible to derive the average absorption and scattering factors of the underlying media by fitting to this data.

21.2.4 Spectroscopy of Homogeneous Turbid Media

The absorption factor, μ_a, depends on the chromophore concentrations, and their extinction coefficients. The predominant endogenous absorbers in tissues are oxy- and deoxyhemoglobin, and water. The scattering factor, μ_s', depends on other tissue properties such as organelle (e.g., mitochondria) concentration and the index of refraction of the background fluids. If the medium is sufficiently homogenous, then by measuring the absorption and scattering coefficients as a function of light wavelength, one generates a set of simultaneous equations that can be solved to yield the concentrations of the tissue chromophores.

The simplest and most commonly used physical model for tissue spectroscopy treats the sample as a semi-infinite medium. In this case the sources and detectors are placed on the "air side" of the tissue surface (see, for example, Figure 21.3). Emission and detection take place through optical fibers placed flush with the surface. The quantity measured in practice at position **r**, time t, and along the direction n is the radiance integrated over the collection solid angle. Within the diffusion approximation, the radiance consists of an isotropic fluence rate ($\Phi(\mathbf{r},t)$) and a directional photon flux ($J(\mathbf{r},t)$) that is proportional to the gradient of Φ.

Diffusion theory for semi-infinite media predicts the reflectivity $R(\rho; \mu_a, \mu_s')$ as a function of ρ, where ρ is the source-detector separation along the sample surface. $R(\rho; \mu_a, \mu_s')$ is derived from photon flux and fluence rate at the boundary[79,80]

$$R(\rho;\mu_a,\mu_s') = C_1\Phi(\rho) + C_2 J_z(\rho) \tag{21.5}$$

where

$$\Phi(\rho) = \frac{1}{4\pi D}\left(\frac{\exp(-\mu_{eff} r_1(\rho))}{r_1(\rho)} - \frac{\exp(-\mu_{eff} r_2(\rho))}{r_2(\rho)}\right) \tag{21.6a}$$

and

$$J_z(\rho) = \frac{1}{4\pi\mu_t}\left[\left(\mu_{eff} + \frac{1}{r_1(\rho)}\right)\frac{\exp\left(-\mu_{eff} r_1(\rho)\right)}{r_1^2(\rho)}\right. \\ \left. + \left(\frac{1}{\mu_t} + 2z_b\right)\left(\mu_{eff} + \frac{1}{r_2(\rho)}\right)\frac{\exp\left(-\mu_{eff} r_2(\rho)\right)}{r_2^2(\rho)}\right] \quad (21.6b)$$

Here, $\mu_t = \mu_a + \mu_s'$, and $\mu_{eff} = [3\mu_a(\mu_a + \mu_s')]^{1/2}$. C_1 and C_2 are constants that depend on the relative refractive index mismatch between the tissue and the detector fiber, and the numerical aperture of the detection fibers. The parameters $r_i(\rho)$ are defined in Figure 21.2. Briefly, $r_1(\rho)$ is the distance from the point of contact of the detector fiber on the tissue surface to the effective source position in the tissue located $1/\mu_t'$ directly beneath the source fiber; $r_2(\rho)$ is the distance between the point of contact of the detector fiber and a point located $1/\mu_t + 2z_b$ directly above the source; z_b is the extrapolated boundary length above the surface of the medium. Here the z-direction has been taken normal to the tissue surface (located at $z = 0$), so that J_z is the directional flux normal to the surface.

The tissue optical properties at a fixed wavelength are derived from the measured reflectance by fitting with Equation 21.5. Many schemes have been developed to search for the optimal parameters;[80–82] their relative success depends on the measurement signal-to-noise ratio and the accuracy of the physical model. When everything works, one obtains a best estimate of the absorption factor and scattering factor at one or more optical wavelengths. We then decompose the absorption coefficient into contributions from different tissue chromophores, i.e.,

$$\mu_a(\lambda) = \sum_i \varepsilon_i(\lambda)\, c_i \,. \quad (21.7)$$

Here the sum is over the different tissue chromophores; $\varepsilon_i(\lambda)$ is the extinction coefficient as a function of wavelength for the ith chromophore and c_i is the concentration of the ith chromophore. The c_i are unknowns to be reconstructed from the wavelength-dependent absorption factors. Three unknowns require measurements at a minimum of three optical wavelengths (generally more, because tissue scattering is also an unknown).

Oxy- and deoxyhemoglobin concentrations (e.g., c_{HbO_2}, c_{Hb}, respectively) along with water concentration are the most significant tissue absorbers in the NIR. They can be combined to obtain blood volume (which is proportional to total hemoglobin concentration ($[c_{Hb} + c_{HbO_2}]$) and blood oxygen saturation (i.e., $[c_{HbO_2}/(c_{Hb} + c_{HbO_2})] \times 100$), which in turn provide useful physiological information. The same schemes are often extended to derive information about exogenous agents such as photodynamic therapy (PDT) drugs, indocyanine green (ICG), etc.; in such cases the effect of these other chromophores is accounted for by adding their contribution to the sum in Equation 21.7.

21.2.5 Imaging in Heterogeneous Media

21.2.5.1 Brief History

Tissue is often quite heterogeneous, so it is natural to contemplate making images with the diffusive waves. While high spatial resolution is desirable (e.g., a few millimeters), resolutions of about 1 cm are useful for many problems. A simple example of the utility of imaging is the early localization of a head injury that causes brain bleeding or hematomas. Tumors are another type of structural anomaly that one wants to detect, localize, and classify. The diffuse optical methods probe a variety of properties associated with tumor growth: larger blood volume resulting from a larger number density and volume fraction of blood vessels residing within the tumor; blood deoxygenation arising from relatively high metabolic activity within the tumor; increased concentration of the intracellular organelles necessary for the energy production associated with rapid growth; and the accumulation of highly scattering calcium precipitates.

Some of these properties may prove helpful in classifying tumors as benign or malignant. In the long term it should be possible to design contrast agents that respond to specific tumor properties. Other types of tissue of interest for functional imaging include the neonatal brain and a variety of animal models. For example, physiological studies of hemodynamics in relation to the oxygen demand probe important changes in the functional brain, especially during mental activity. In Section 21.4 we describe current research that investigates many of the clinical issues just outlined.

Optical characterization of the heterogeneous tissues has been attempted since 1929[83] when the term *diaphanography* was applied to shadowgraphs of breast tissue. This class of transillumination measurement was renewed in the early 1980s.[84–95] Even in the region of low tissue absorption, however, the high degree of tissue scattering distorted spectroscopic information and blurred optical images as a result of the large distribution of photon pathways through the tissue. Widebeam transillumination proved largely inadequate for clinical use because the two-dimensional "photographic" data were poorly suited for image reconstruction. The mathematical modeling of light transport in tissues was not developed sufficiently for optical tomography to be readily employed.

The diffusion approximation now provides a tractable basis for tomographic approaches to image reconstruction using highly scattered light. Tomographic methods crucial for recovery of information about breast heterogeneities were not employed in the early transillumination patient studies. Several approaches have been developed for diffuse optical tomography; these include: backprojection methods,[96,97] diffraction tomography in k-space,[98–101] perturbation approaches,[102–107] the Taylor series expansion approach,[108–113] gradient-based iterative techniques,[114] elliptic systems method (ESM),[115,116] and Bayesian conditioning.[117] Backprojection methods, borrowed from CT, produce images quickly and use few computational resources. However, they lack quantitative information and rely on simple geometries. Perturbation approaches based on Born or Rytov approximations can use analytic forms or iterative techniques based on numerical solutions. The analytic forms are relatively fast, but require the use of simple boundary conditions and geometries, and generally underestimate the properties of the perturbations. The numerical solutions are relatively slow and computationally intensive; however, in principle, realistic boundaries present no significant limitations for these methods.

21.2.5.2 Formulation of the Imaging Problem

In this section we formulate the imaging problem in the frequency domain. The starting point of this analysis is the time-independent form of the diffusion equation (Equation 21.1), where we have divided out all of the $e^{i\omega t}$ dependencies:

$$\nabla \cdot D(\mathbf{r})\nabla\Phi(\mathbf{r}) - \left(v\mu_a(\mathbf{r}) - i\omega\right)\Phi(\mathbf{r}) = -vS(\mathbf{r},\omega)\,. \tag{21.8}$$

The problem is difficult because the diffusion coefficient and the absorption coefficient vary with spatial position. We write $D(\mathbf{r}) = D_o + \delta D(\mathbf{r})$, and $\mu_a(\mathbf{r}) = \mu_{ao} + \delta\mu_a(\mathbf{r})$; here D_o and μ_{ao} are constant, "background" optical properties. The source can have any form, but typically we assume point sources of the form $A\delta(\mathbf{r} - \mathbf{r}_s)$.

The goal of diffuse optical imaging is to derive $D(\mathbf{r})$ and $\mu_a(\mathbf{r})$ from measurements of $\Phi(\mathbf{r})$ on the sample surface. Two common forms are used for $\Phi(\mathbf{r})$ in the formulation of the inversion problem. The Born-type approach writes $\Phi(\mathbf{r}) = \Phi_o(\mathbf{r}) + \Phi_{sc}(\mathbf{r})$; traditionally one can view $\Phi_o(\mathbf{r})$ as the incident wave and $\Phi_{sc}(\mathbf{r})$ as the wave produced by the scattering of this incident wave off the absorptive and diffusive heterogeneities. The Rytov approach writes $\Phi(\mathbf{r}) = \Phi_o(\mathbf{r})\exp[\Phi_{sc}(\mathbf{r})]$. We will focus on the Born approximation for our analysis, and indicate when possible the corresponding Rytov results.

We next substitute $D(\mathbf{r})$, $\mu_a(\mathbf{r})$, and $\Phi(\mathbf{r}) = \Phi_o(\mathbf{r}) + \Phi_{sc}(\mathbf{r})$ into Equation 21.8 to obtain a differential equation for $\Phi_{sc}(\mathbf{r})$ with general solution:

$$\Phi_{sc}(\mathbf{r}_d,\mathbf{r}_s) = \int\left(\frac{-v\delta\mu_a(\mathbf{r})}{D_o}\right)G(\mathbf{r}_d,\mathbf{r})\Phi(\mathbf{r},\mathbf{r}_s)d\mathbf{r} + \int\left(\frac{\delta D(\mathbf{r})}{D_o}\right)\nabla G(\mathbf{r}_d,\mathbf{r})\cdot\nabla\Phi(\mathbf{r},\mathbf{r}_s)d\mathbf{r}\,. \tag{21.9}$$

Here $\mathbf{r}_s$ is the source position, $\mathbf{r}_d$ is the detector position, $\mathbf{r}$ is a position within the sample. The integration is over the entire sample volume. $G(\mathbf{r},\mathbf{r}')$ is the Green's function associated with Equation 21.8. Examination of Equation 21.9 reveals some of the intrinsic challenges of the inverse problem. In a typical experiment one measures Φ on the sample surface and then extracts Φ_{sc} on the surface by subtracting Φ_0 from Φ. The problem of deriving $\delta\mu_a(\mathbf{r})$ and $\delta D(\mathbf{r})$ from Φ is intrinsically nonlinear because Φ and G are nonlinear functions of $\delta\mu_a(\mathbf{r})$ and $\delta D(\mathbf{r})$.

The Linearized Problem

The simplest and most direct route to inverting Equation 21.9 starts by replacing Φ by Φ_0 and G by G_0. Here Φ_0 and G_0 are solutions of the homogeneous version of Equation 21.8 with $D(\mathbf{r}) = D_0$, and $\mu_a(\mathbf{r}) = \mu_{a0}$. This approximation is good when $\Phi_0 << \Phi$, and when the perturbations are very small compared to the background. It is also important that we have accurate estimates of D_0 and μ_{a0}. In this case, Equation 21.9 is readily discretized in Cartesian coordinates and written in the following form:

$$\Phi_{sc}(\mathbf{r}_d,\mathbf{r}_s) = \sum_{j=1}^{NV}\left(W_{a,j}\delta\mu_a(\mathbf{r}_j) + W_{s,j}\delta D(\mathbf{r}_j)\right). \tag{21.10}$$

The sum is taken over NV volume elements (i.e., voxels) within the sample; the absorption and scattering weights are, respectively, $W_{a,j} = G_0(\mathbf{r}_d,\mathbf{r}_j)\,\Phi_0(\mathbf{r}_j,\mathbf{r}s)\,(-v\Delta x\,\Delta y\,\Delta z/D_0)$, and $W_{s,j} = \nabla G_0(\mathbf{r}_d,\mathbf{r}_j)\cdot\nabla\Phi_0(\mathbf{r}_j,\mathbf{r}_s)\,(\Delta x\,\Delta y\,\Delta z/D_0)$. In any practical situation there will be NS sources and ND detectors, and so there will be up to $NM = NS \times ND$ measurements of Φ on the sample surface. For the multisource-detector problem one naturally transforms Equation 21.10 into a matrix equation, i.e.,

$$\left[\mathrm{W}_{a,ij},\mathrm{W}_{s,ij}\right]\left\{\delta\mu_a(\mathbf{r}_j),\delta D(\mathbf{r}_j)\right\}^T = \left\{\Phi_{sc}(\mathbf{r}_d,\mathbf{r}_s)_i\right\}. \tag{21.11}$$

Here, the index i refers to source-detector pair, and the index j refers to position within the sample. The perturbation vector $\{\delta\mu_a(\mathbf{r}_j), \delta D(\mathbf{r}_j)\}^T$ is $2NV$ in length, the measurement vector $\{\Phi_{sc}(\mathbf{r}_d,\mathbf{r}_s)_i\}$ is NM in length, and the matrix [W] has dimensions $NM \times (2NV)$. In the Rytov scheme, the formulation in the weak perturbation limit is almost exactly the same, except that $W_{a,ij} = G_0(\mathbf{r}_d,\mathbf{r}_j)\,\Phi_0(\mathbf{r}_j,\mathbf{r}_s)(-v\Delta x\,\Delta y\,\Delta z/\Phi_0(\mathbf{r}_d,\mathbf{r}_s)\,D_0)$, $W_{s,j} = \nabla G_0(\mathbf{r}_d,\mathbf{r}_j)\cdot\nabla\Phi_0(\mathbf{r}_j,\mathbf{r}_s)\,(\Delta x\,\Delta y\,\Delta z/\Phi_0(\mathbf{r}_d,\mathbf{r}_s)\,D_0)$, and the vector $\{\Phi_{sc}(\mathbf{r}_d,\mathbf{r}_s)_i\}$ is set equal to $\{\ln[\Phi(\mathbf{r}_d,\mathbf{r}_s)/\Phi_0(\mathbf{r}_d,\mathbf{r}_s)]_i\}$ rather than $\{[\Phi(\mathbf{r}_d,\mathbf{r}_s) - \Phi_0(\mathbf{r}_d,\mathbf{r}_s)]_i\}$. The Rytov scheme has some experimental advantages because it is intrinsically normalized (the Born scheme, however, can be modified so that it is normalized in essentially the same way); the major approximations of the Rytov scheme are associated with the gradients of Φ, in particular that $(\nabla\Phi_{sc})^2$ is small relative to the perturbation terms in Equation 21.9. Thus both Born and Rytov approaches give rise to an inverse problem of the form [W] $\{x\} = \{b\}$; the unknown vector $\{x\}$ can be determined from this set of linear equations by a number of standard mathematical techniques. The numerical elements in [W] are often assigned in simple geometries using analytic forms of G_0 and Φ_0 (e.g., Equation 21.3 and variants), or more generally by numerically solving Equation 21.8 and its Green's function analog for Φ_0 and G_0.

The Nonlinear Problem

The linear formulation described above works well when perturbations are small and isolated, and when the background media are relatively uniform. However, Equation 21.9 is intrinsically nonlinear because Φ and G are also functions of the variables we are trying to determine by inversion. The most broadly useful image reconstruction schemes are iterative. These approaches follow similar algorithms: (1) the optical properties (μ_a and D) are initialized; (2) the forward problem is solved; (3) a chi-squared is calculated and convergence is checked; (4) the inverse problem is set up; (5) the inverse problem is solved; (6) the optical properties are updated and a return to step 1 occurs.

The forward problem is defined as calculating the diffuse photon density, $\Phi_0(\mathbf{r},\mathbf{r}_s)$, for each source position $\mathbf{r}_s$ and is typically found using finite elements or finite difference methods using Equation 21.8. The boundary conditions are defined as:

$$\frac{\partial \Phi_C}{\partial \hat{n}} = -\alpha \Phi_C, \quad \alpha = \frac{\left(1 - R_{eff}\right)}{\left(1 + R_{eff}\right)} \frac{3\mu_s'}{2}. \tag{21.12}$$

R_{eff} is the effective reflection coefficient and can be approximated by: $R_{eff} = -1.440n^{-2} + 0.710n^{-1} + 0.668 + 0.0636n$, $n = n_{in}/n_{out}$ the relative index of refraction.[55] The chi-squared (χ^2) is generally defined as:

$$\chi^2 = \sum_{NM} \left(\frac{\Phi_M(r_d^i) - \Phi_C(r_d^i)}{\sigma^i} \right)^2. \tag{21.13}$$

Here NM = number of measurements, M = measured, C = calculated, $\mathbf{r}_d^i$ is the ith detector position, and σ^i is the ith measurement error. By comparing χ^2 to some defined ε, a convergence criterion is defined and checked.

We then need a way of updating the optical properties from their previous values. A standard Taylor method expands Φ_C about its assumed optical property distribution, which is a perturbation away from another distribution presumed closer to the true value. In particular we set the measured photon density wave for each source-detector pair equal to the calculated photon density wave at the corresponding source-detector pair plus the first-order Taylor series perturbation expansion terms in μ_a and D, i.e., $\Phi_M = \Phi_C + (\partial\Phi_C/\partial\mu_a)\Delta\mu_a + (\partial\Phi_C/\partial D)\Delta D$.

The inverse problem is defined from this relationship:

$$[J]\{\Delta\mu_a, \Delta D\}^T = -\left\{\Phi_M(\mathbf{r}_d) - \Phi_C(\mathbf{r}_d)\right\}. \tag{21.14}$$

Here $[J] = [\partial\Phi_C/\partial\mu_a, \partial\Phi_C/\partial D]$ is called the Jacobian. The Jacobian matrix will have the following entries:

$$\left[\frac{\partial \Phi_C}{\partial \mu_a}\right]_{ij} = \frac{-v\Delta x\Delta y\Delta z}{D_o} G(\mathbf{r}_{di}, \mathbf{r}_j)\Phi_C(\mathbf{r}_j, \mathbf{r}_{si}) \tag{21.15a}$$

$$\left[\frac{\partial \Phi_C}{\partial D}\right]_{ij} = \frac{\Delta x\Delta y\Delta z}{D_o} \nabla G(\mathbf{r}_{di}, \mathbf{r}_j) \cdot \nabla \Phi_C(\mathbf{r}_j, \mathbf{r}_{si}). \tag{21.15b}$$

It is illuminating at this point to compare Equation 21.14 with Equation 21.11. The two expressions are essentially the same if we associate Φ_M with Φ, Φ_C with Φ_o, $\Delta\mu_a$ with $\delta\mu_a$, ΔD with δD, and if we use the true Green's function G rather than G_o. The same set of substitutions in the Rytov formulation gives a Rytov version of the nonlinear inversion scheme. Thus the iterative formulation of the inverse problem is based on the same underlying integral relationship (Equation 21.9), and one readily sees that each step of the "nonlinear" iteration process is a linear inverse problem of the form [J] {x} = {b}.

21.2.5.3 Methods for Solving the Inverse Problem

The inverse problem may be solved using a wide range of methods (an excellent review of these methods was given by Arridge[118]). The solution method chosen depends in part on the determination of the *implicit* or *explicit* Jacobian. For the explicit Jacobian two methods are commonly employed: the Newton-Raphson and the conjugate gradient techniques. It is also possible to combine these methods with Bayesian conditioning or regularization to improve reconstruction. For the implicit Jacobian, the methods of choice are the gradient-based iterative technique and ART (algebraic reconstruction technique).

There are essentially two ways to construct the Jacobian, [J] *explicitly*: direct and adjoint. The *direct* approach explicitly takes the derivative of the forward problem (Equation 21.8) with respect to the optical properties to determine the Jacobian. For example, suppose [A]{Φ_C} = {S} is the forward problem; here [A] is the operator on the left side of Equation 21.8 and {S} is the source on the right side of Equation 21.8.

Then the equation $[A]\{\partial\Phi_C/\partial\mu_a\} = \{\partial S/\partial\mu_a\} - [\partial A/\partial\mu_a]\{\Phi_C\}$ enables one to compute $\partial\Phi_C/\partial\mu_a$ (and a similar forward problem enables the computation of $\partial\Phi_C/\partial D$).[108] This approach is optimal with finite elements; because the numerical formulation lends itself easily to taking the derivative of $[A]$. Φ_C, $[A]$ and $[A]^{-1}$ are updated on each iteration. The *adjoint* approach solves the forward problem $[A]\{\Phi_C\} = \{S\}$ to determine Φ_C, and an adjoint problem $[A^*]\{G\} = \{S'\}$ to determine Green's function $G(\mathbf{r}_d,\mathbf{r})$ due to a unit source at the detector position.[1,102–105,107,119,120] G and Φ_C then fix the elements of $[J]$ according to Equation 21.15. Both Φ_C and G are updated at each iteration. The impact of the two different approaches on convergence and accuracy is not well understood. However, from the computational perspective, for each iteration the direct approach requires 3NS solves per iteration, while the adjoint Born or Rytov approach requires *NS* plus *ND* solves per iteration.

The inverse problem, $[J]\{\Delta\mu_a, \Delta D\}^T = \{\Phi_M - \Phi_C\}$, which is also a matrix equation, is significantly more costly than these other subproblems because the Jacobian is a full nonsquare matrix $\{NM \times 2NV\}$. However, the inverse problem only needs to be solved once per iteration cycle. The Jacobian is ill-conditioned and is thus singular or close to singular, which makes it difficult to invert directly. Generally, the approach to address these issues is twofold. First, the matrix is made square by multiplying the inverse problem by the transpose of the Jacobian, i.e.,

$$[J]^T[J]\{\Delta\mu_a, \Delta D\}^T = [J]^T\{\Phi_M - \Phi_C\}. \tag{21.16}$$

Unfortunately, by squaring the Jacobian the equation becomes even more ill conditioned. This problem is solved by regularization[121,122] so that the equation becomes

$$\left([J]^T[J] + \lambda[C]^T[C]\right)\{\Delta\mu_a, \Delta D\}^T = [J]^T\{\Phi_M - \Phi_C\}. \tag{21.17}$$

Here λ is called the regularization parameter and $[C]$ is the regularizing operator, which is sometimes taken to be the identity matrix. The regularization parameter generally is related to the measurement signal-to-noise. It is a theoretical "knob" that can be adjusted and it will affect image quality by introducing a trade-off between spatial resolution and contrast.[122,123] Nevertheless, its use converts the inverse problem into a readily solvable problem. $\{\Delta\mu_a, \Delta D\}^T$ can now be determined using Equation 21.17 and any number of mathematical techniques that solve systems of linear equations. A particularly useful and common solution scheme is the conjugate gradient method.

A qualitatively different scheme due to Arridge involves the implicit determination of the Jacobian. Briefly, this technique utilizes the Born or Rytov approximation for the inverse problem, and has at least two known solution methods: gradient-based iterative technique and ART (algebraic reconstruction technique). The Jacobian is not calculated; instead an objective function (e.g., a chi-square function) is defined whose gradient, for example, can be used to derive subsequent search directions (see the original papers, References 114 and 118, for details.) Note that the implicit formulation is particularly attractive for experimental systems that rely on many detectors rather than many sources.

21.2.5.4 Challenges for Implementation

The main barrier for full three-dimensional reconstruction is the significant memory and processing time it requires. There are three costly steps of the algorithms: (1) solving the forward problem for each source position, (2) determining the Jacobian, and (3) solving the inverse problem. The forward problem requires the solution of a matrix equation banded in finite difference or sparse in finite elements. The solvers in three-dimensional reconstruction are necessarily iterative because direct solvers require very large storage space for full matrices. Subsequently, multiple source positions demand multiple forward solves. Determination of the Jacobian requires additional matrix equation solutions. For explicit determination, the Green's function for each detector position is needed or the vectors $\partial\Phi_C/\partial\mu_a$ and $\partial\Phi_C/\partial D$ are needed.

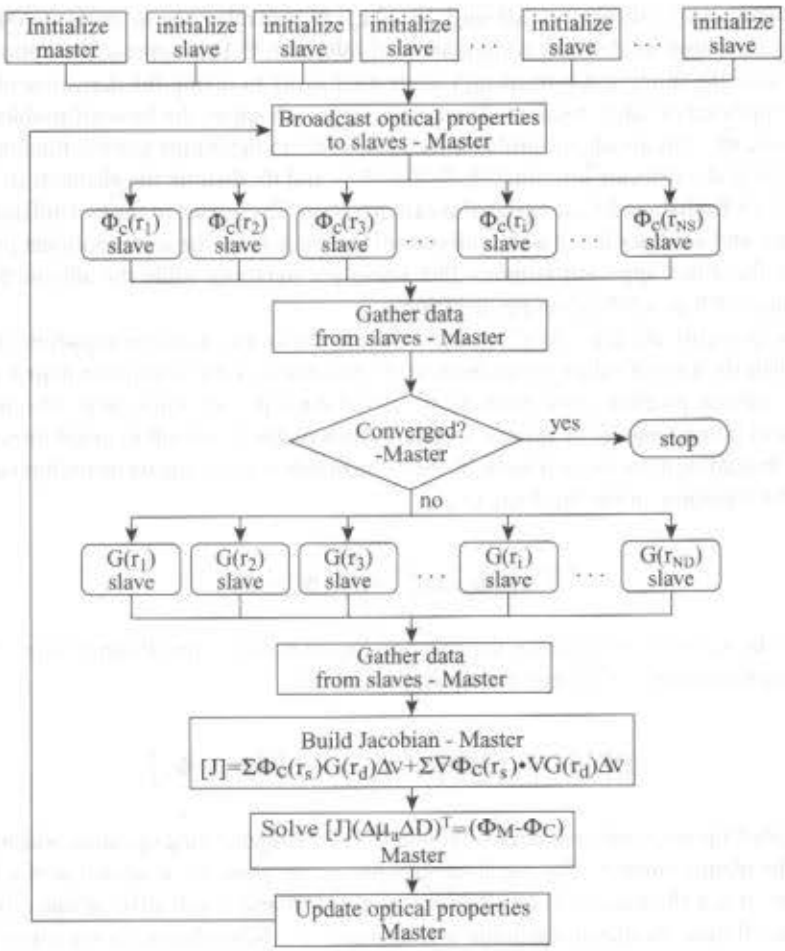

FIGURE 21.4 Schematic of the University of Pennsylvania algorithm for image reconstruction using parallel computing. In the first step each node has its own set of arrays and variables that are initialized. The master must initialize the Jacobian array, the forward solution vector array, and the Green's function vector array. In the second step the master sends out the optical properties, which (in the first iteration) are just the background values. In the third step, the slaves calculate the solutions to the forward problem; *NS* slaves are used in this step. The solution vectors are then returned to the master and at this point the master checks for convergence. If convergence has not been achieved then the slaves calculate the solutions to the Green's function; *ND* slaves are used in this step. The solution vectors are returned to the master and the Jacobian is determined. Next the master solves the inverse problem, in this case by using a spatially variant regularized conjugate gradient optimization method. Finally, the optical properties are updated on the master and the algorithm repeats until convergence has been achieved.

Consider a system with one frequency — *NS* sources and *ND* detectors; assume further that all the detectors are used for each source. The number of measurements is $NM = NS \times ND$. For each iteration we require *NS* forward solves and, depending on the Jacobian determination, either *ND* Green's function or $2NS$ solves for the vectors $\partial\Phi_C/\partial\mu_a$ and $\partial\Phi_C/\partial D$ (implicit would require *NS* solves). The final costly step of the algorithm is the solution of the inverse problem. However, the inverse problem only needs to be solved once per iteration cycle. For many practical problems the calculations take a long time, and limited memory is available to store the Jacobian explicitly. An important solution to this large-scale computational problem is parallel computing — the execution of many computations at one time using many processors. It has been used successfully in areas of medical imaging, such as positron emission tomography (PET),[124–128] single photon emission computed tomography (SPECT),[129,130] computed tomography (CT),[131–133] electrical impedance tomography (EIT),[134] and optical sectioning microscopy

(OSM).[135] It is just beginning to catch on in the diffuse optical tomography (DOT) community.[136,137] In Figure 21.4, we illustrate how the problem is parallelized at the University of Pennsylvania.

21.2.6 Diffusion of Light Correlations: Blood Flow

Thus far our discussion has centered around the determination of tissue absorption and scattering properties. Among other things, these measurements provide access to concentrations of oxygenated and deoxygenated hemoglobin. Even more information, however, is impressed upon these diffusing light fields. Speckle fluctuations of the scattered light are sensitive to the motions of scatterers such as red blood cells.

The means for using light fluctuations and light frequency shifts to study motions have appeared with numerous names over the years.[138–158] In most of these experiments the quantity of interest is the electric field temporal autocorrelation function $G_1(\mathbf{r},\tau) = \langle E(\mathbf{r},t)\, E^*(\mathbf{r}, t+\tau)\rangle$ or its Fourier transform. Here the angle brackets $\langle\ \rangle$ denote ensemble averages or averages over time for most systems of practical interest. τ is called the correlation time. The field correlation function is explicitly related to the motions of scatterers within the samples that we study.

The study of these motions in deep tissues is possible because the electric field temporal autocorrelation function for light traveling in highly scattering media also obeys a diffusion equation.[152] In steady-state (i.e., $\omega = 0$) and in homogeneous media, this correlation diffusion equation is quite simple:

$$\left(D\nabla^2 - v\mu_a - \alpha k_0^2 \mu_s' \left\langle \Delta r^2(\tau)\right\rangle/3\right) G_1(\mathbf{r},\tau) = -vS(\mathbf{r})\,. \tag{21.18}$$

Here k_0 is the wavevector of the photons in the medium and $\langle \Delta \mathbf{r}^2(\tau)\rangle$ is the mean-square displacement in time τ of the scattering particles (e.g., blood cells); it can have different forms depending on the nature of the particle motion and can also vary with position. $S(\mathbf{r})$ is the source light distribution, and α represents the fraction of photon scattering events in the tissue that occur from moving cells or particles.

Notice that, for $\tau \to 0$, $\langle \Delta \mathbf{r}^2(\tau)\rangle \to 0$, and Equation 21.18 reduces to the steady-state diffusion equation for diffuse photon fluence rate (i.e., Equation 21.8 with $\omega = 0$). Notice also that the homogenous version of Equation 21.18 can be recast as a Helmholtz-like equation for the temporal field autocorrelation function, $G_1(\mathbf{r},\tau)$, i.e.,

$$\left(\nabla^2 + K^2(\tau)\right) G_1(\mathbf{r},\tau) = -S(\mathbf{r})/D\,, \tag{21.19a}$$

$$K^2(\tau) = \left(-v/D\right)\left(\mu_a + \alpha k_0^2 \mu_s' \left\langle \Delta r^2(\tau)\right\rangle/3\right). \tag{21.19b}$$

For an infinite homogenous medium with a point source at the origin, this equation will also have the well known spherical-wave solution, i.e., $\sim[\exp\{-K(\tau)\mathbf{r}\}/D4\pi\mathbf{r}]$.

The mean-square displacement $\langle \Delta \mathbf{r}^2(\tau)\rangle = 6D_B\tau$ for organelles or cells undergoing Brownian motion with "particle" diffusion coefficient D_B. For the important case of random flow that can arise in the tissue vasculature, $\langle \Delta \mathbf{r}^2(\tau)\rangle = \langle V^2\rangle\tau^2$, where $\langle V^2\rangle$ is the second moment of the cell speed distribution. In the latter case the correlation function will decay exponentially as τ.

Multidistance measurements of $G_1(\mathbf{r},\tau)$ provide dynamical information about the motions within the sample in exactly the same way that diffusive waves provide information about scattering and absorption properties. The layout of the sources and detectors is similar to the diffusive wave schemes, but the correlation measurements are a little more complex. For the measurements, one needs a special piece of equipment called an autocorrelator, which takes the detector output and uses the photon arrival times to compute $G_1(\mathbf{r},\tau)$ or (more precisely) its light *intensity* analog.

The entire set of formalisms for imaging outlined in Sections 21.2.5.2 and 21.2.5.3 is applicable to diffuse light temporal correlations. The technique is attractive because it enables us to measure the blood

flow (i.e., $\langle \Delta \mathbf{r}^2(\tau) \rangle$) within deep tissues. The ability to measure relative changes concurrently in blood flow, hemoglobin concentration, and hemoglobin oxygenation within a single instrument makes possible a range of cerebral studies in animal models and in infants and neonates (see References 159 through 161).

21.2.7 Contrast Agents

The use of contrast agents in DOT and spectroscopy for disease diagnostics and for probing tissue functionality follows established clinical imaging modalities such as magnetic resonance imaging (MRI),[162–164] ultrasound,[164–166] and x-ray computed tomography (CT).[164,167,168] Contrast agent administration provides for accurate difference images of the same heterogenous tissue volume under nearly identical experimental conditions; this approach often yields superior diagnostic information. Although contrast agents most commonly induce changes in absorption, recently fluorescent/phosphorescent agents have also been considered as means to increase specificity and sensitivity for tumor detection and imaging.[77,169–184] In addition to concentration changes, fluorophore lifetime is sensitive to physiological environment, for example, through oxygen quenching or pH. Most contrast agent schemes rely on the fact that the exogenous macromolecular structures accumulate preferentially in abnormal tissues.

21.2.7.1 Fluorescent Contrast Agents

A chapter in this handbook already reviews contrast agents in photon migration, so we will be very brief. (Our discussion follows from References 185 through 187.) Suppose a heterogeneous turbid medium with fluorophore distribution $N(\mathbf{r})$ is excited by an excitation diffusive wave, $\Phi(\mathbf{r},\mathbf{r}_s)$, emitted from $\mathbf{r}_s$ and whose optical wavelength is in the absorption band of the fluorophore. A fluorescent diffuse photon density wave, $\Phi_\beta(\mathbf{r},\mathbf{r}_s)$, is produced in the medium, and

$$\Phi_\beta(\mathbf{r},\mathbf{r}_s) = \int G_\beta(\mathbf{r},\mathbf{r}')T(\mathbf{r}')\Phi(\mathbf{r}',\mathbf{r}_s)d\mathbf{r} \tag{21.20a}$$

where

$$T(\mathbf{r}') = \varepsilon \frac{\tau}{\tau_o} \frac{\eta N(r)}{1-\omega\tau}. \tag{21.20b}$$

The integration is over the sample volume. Here $T(\mathbf{r})$ is a fluorescence transfer function, which depends on the fluorophore radiative and total lifetimes, τ_o and τ respectively, the source modulation frequency ω, the fluorophore extinction coefficient ε, the fluorescence quantum yield η, and the fluorophore distribution $N(\mathbf{r})$. In principle, τ_o and τ (and even ε and η) can also depend on position. The Green's function $G_\beta(\mathbf{r}, \mathbf{r}')$ is derived with a diffusion equation (Equation 21.8) for the fluorescent diffuse photon density wave at the emission wavelength, i.e., the absorption and scattering coefficients in this diffusion equation are defined at the fluorescent emission wavelength. Equation 21.20 is very similar to the equations we inverted in Sections 21.2.5.2 and 21.2.5.3. However, it is deceptively simple because heterogeneity information is embedded in Φ and G_β, in addition to N and τ. Nevertheless, it can be inverted numerically using similar techniques.

21.2.7.2 Differential Absorption

In these measurements optical data are typically obtained before and after administration of the absorbing optical contrast agent (e.g., the intraveneous administration of ICG. In principle, DOT images taken before and after administration may be reconstructed and subtracted; however, in practice a more robust approach derives images of the differential changes due to the extrinsic perturbtion. In the latter case experimental measurements use the exact same geometry within a short time of one another, thereby minimizing positional and movement errors and instrumental drift. Furthermore, the use of differential

measurements eliminates systematic errors associated with the different medium often required to calibrate operational parameters of the instrument or to provide a baseline measurement for independent reconstructions. Finally, the effect of surface absorbers such as hair- or skin-color variation is also minimized.

The main analytical difficulties of the differential approach arise because the media are inhomogeneous. Thus the total diffuse light field in the contrast agent perturbation problem does not separate into a homogeneous background field and a scattered field in a straightforward way. Furthermore, the average background optical properties, particularly the absorption, can change as a result of contrast agent administration.

In the typical experiment, relative absorption changes are much larger than scattering changes and one can ignore the relative changes in scattering. Under these circumstances the differential signal $\Delta\Phi$, can be related to the differential absorption $\Delta\mu_a$ via the integral relation:[188]

$$\Delta\Phi(\mathbf{r},\mathbf{r}_s) = \int W_a'(\mathbf{r},\mathbf{r}',\mathbf{r}_s)\Delta\mu_a(\mathbf{r}')d\mathbf{r} + C\,. \tag{21.21}$$

Here W_a' is a weight function very similar to the functions discussed in Section 21.2.5.2. C is a correction; it is an integral that depends on source-detector geometry and on the weight function before and after administration of the contrast agent. For many geometries (e.g., the transmission geometry) C is small and can be ignored. In those cases we can directly invert Equation 21.21 according to the ideas described in Sections 21.2.5.2 and 21.2.5.3, and thus obtain the differential absorption changes directly from difference measurements.

21.3 Instrumentation

The basic imaging geometry for diffuse optical tomography consists of a set of distinguishable point-like sources and a set of photodetectors, each covering a small area of <10 mm^2 on the surface of the medium. In general some type of source encoding strategy must be used so that the origin of the detected signals can be traced to specific sources. In this way, measurements with differing spatial sensitivities are obtained, and an image can be reconstructed.

There are three common measurement geometries: (1) planar transillumination measurements, (2) cylindrical measurements, and (3) reflectance measurements. All three are used for breast imaging (transillumination,[10–13,189] cylindrical,[15,190–192] and reflectance.[119,137,193]). The cylindrical and reflectance geometries are used for imaging animals, human baby heads,[28,194–197] and limbs on the human body (e.g., arm or leg). The reflectance geometry is used for imaging human adult heads.[139,198–200]

In Section 21.2.2 we identified three diffuse light excitation schemes: (1) illumination by subnanosecond pulses of light, (2) CW illumination, and (3) radio-frequency (RF) amplitude-modulated illumination. Short-pulse systems[201–205] detect the temporal distribution of photons as they leave the tissue. The shape of the distribution provides information about tissue optical parameters. Although these systems provide the most information per source-detector pair for characterizing optical properties, their relatively poor signal-to-noise ratio (SNR) leads to longer image acquisition times (typically a few minutes in systems used today).

CW systems[195,206–208] emit light of constant intensity or amplitude. (Sometimes the emitted intensity is amplitude modulated at frequencies less than a few tens of kilohertz.) Detectors measure the amplitude of the light transmitted through the tissue. These systems are simple to build and provide fast image rates (presently up to 100 Hz), but their lack of temporal information makes quantitation of tissue absorption and scattering more difficult. In RF systems[209–211] the light source intensity is amplitude modulated at frequencies of tens to hundreds of megahertz. Information about the absorption and scattering properties of tissue is obtained by recording amplitude decay and phase shift (delay) of the detected signal with respect to the incident wave.[211,212] These systems offer the fast image acquisition rate of CW systems and contain information sufficient for quantitative characterization of absorption and

TABLE 21.1 Comparison of Relative Advantages and Disadvantages of Time-Domain, Frequency-Domain, and Continuous-Wave Instrumentation

Instrumentation	Advantages	Disadvantages
Time-Domain	Full temporal impulse response Quantitative	Difficult to maintain Expensive optoelectronics
Frequency-Domain	Diffusive wave phase and amplitude Faster than time-domain Lower cost than time-domain	Difficult RF electronics
Continuous-Wave	Lowest cost Easy electronics Fastest Accurate for differential measurements of optical properties	Diffuse light amplitude only Less accurate for extimates of absolute optical properties

scattering optical properties. The advantages and disadvantages of the three systems are outlined in Table 21.1.

In DOT it is desirable to make a large number of measurements for image reconstruction in a short period of time so that the data are not confounded by physiological or movement artifacts. The balance between number of measurements and image acquisition time is dictated by application. CW systems are popular for imaging spatial variations of absorption changes on timescales of seconds to minutes, for example, imaging muscle[213,214] and brain activation.[195,196,198] CW systems usually have the best SNR and lend themselves well to several encoding strategies enabling massively parallel measurements. Furthermore, although CW systems are poor at quantifying static absorption and scattering properties uniquely, they excel at quantifying spectroscopic changes in absorption and scattering, particularly when *a priori* knowledge of the spectroscopic features is available. On the other hand, RF and time-domain systems are popular for imaging static optical properties when quantitative accuracy is required and when data acquisition times of one to several minutes are acceptable.

21.3.1 Source Encoding Strategies

If cost is not an issue, then increasing the number of parallel detectors or detection systems is a straightforward approach to increasing the number of measurements per unit time. Often, however, measurements with multiple source wavelengths and source positions are desired. In this case an encoding strategy enabling the separation of source wavelengths and positions must be employed. The encoding strategies currently used in CW systems and applicable to RF systems are switched-source time-division multiplexing (SS-TDM), phase-division multiplexing (PDM), pulse-modulated time-division multiplexing (PM-TDM), frequency-division multiplexing (FDM), and wavelength-division multiplexing (WDM). SS-TDM and WDM are applicable to time-domain imaging systems as well.

For SS-TDM, sources are modulated at the same frequency and cycled through consecutively; the detectors synchronously obtain the source signal through their own demodulators. This is the easiest system to design and build. Because at any given time only a single source illuminates the sample, interchannel crosstalk is low, and simple circuit construction techniques (point-to-point wiring, Protoboards, etc.) can be used successfully.

For PDM, two sources are modulated with a square-wave at the same frequency, but in phase quadrature (i.e., at a 90° phase difference). Each of the detectors synchronously detects each source through two separate demodulators and low-pass filters, each of which is "tuned" to the in-phase source. Source pairs can then be cycled through consecutively. This is an easy system to design and build, but component layout affects performance, particularly interchannel crosstalk.

For PM-TDM, M sources are cycled on and off in sequence, but at a rapid (~kHz) rate. For N detectors, each source is synchronously detected through individual demodulators, each of which is time-gated to

one source. This approach has all the benefits of SS-TDM, but with no temporal skew. The system can be difficult to design and construct due to the complex interdigitation and fast switching speeds. Because only one source operates at any one time, the background level is very low.

For FDM, each of the sources is modulated at one of a number of anharmonically related frequencies (to minimize the effects of intermodulation distortion). For each of the detectors, the sources are demodulated coherently (synchronous detection) or incoherently (envelope detection). This is the most complex system to design and build due to the high potential for interchannel crosstalk. The high background flux arising because all sources are on simultaneously raises the shot noise floor and can saturate photo-detectors. However, because each source is "on" all the time, the scheme is more parallel than the sequential approaches described previously.

WDM simply uses bandpass optical filters in front of the photodetectors to distinguish different wavelength sources. This method can be used in combination with any of the encoding strategies described earier to distinguish light from different spatial locations.

21.3.1.1 Continuous-Wave Imaging System

As an example of the CW imaging system, we consider one used at the Massachusetts General Hospital-Nuclear Magnetic Resonance (MGH-NMR) Center. This system employs the FDM scheme to detect 32 lasers with 32 detectors (see Figure 21.5). At present, the 32 lasers are divided into 16 lasers at 690 nm and 16 at 830 nm. These 16 laser pairs are fiber coupled and deliver light to 16 positions on the medium to be imaged. The detectors are avalanche photodiodes (APDs, Hamamatsu C5460-01). A master clock generates the 32 distinct frequencies between 6.4 and 12.6 kHz in approximately 200-Hz steps. These frequencies are then used to drive the individual lasers with current stabilized square-wave modulation. Following each APD module is a bandpass filter, cut-on frequency of ~500 Hz to reduce 1/f noise and the 60-Hz room light signal, and a cut-off frequency of ~16 kHz to reduce the third harmonics of the square-wave signals. After the bandpass filter is a programmable gain stage to match the signal levels with the acquisition level on the analog-to-digital converter within the computer. Each detector is digitized at ~45 kHz and the individual source signals are then obtained by use of a digital bandpass filter — for example, a discrete Fourier transform or an infinite-impulse-response filter.

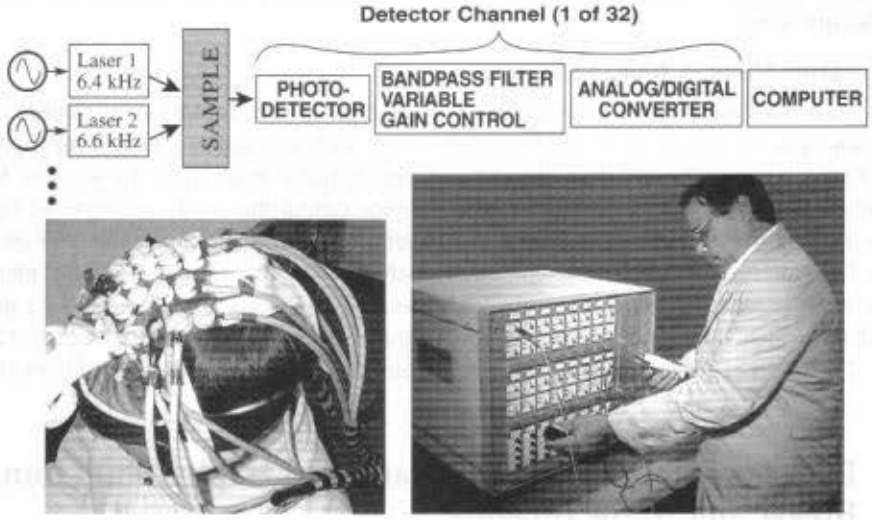

FIGURE 21.5 The MGH-NMR Center CW imaging system with 32 lasers and 32 detectors along with a block diagram indicating the frequency encoded sources and electronic processing steps from the photodetector to the computer memory.

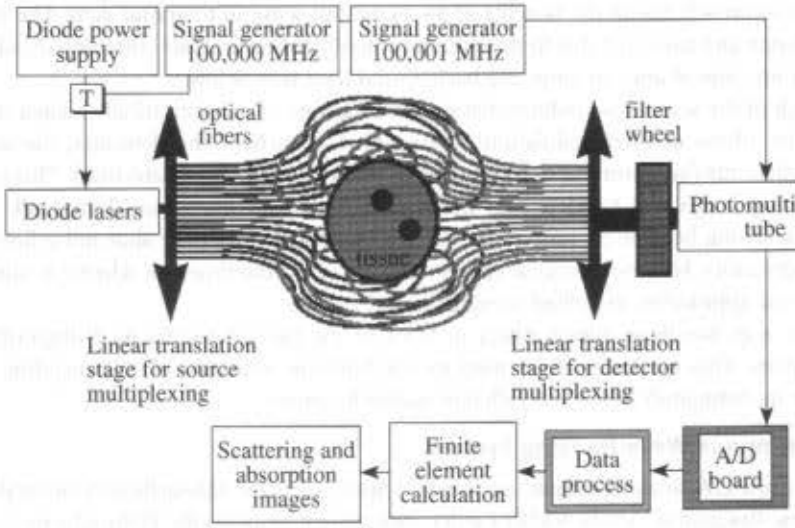

FIGURE 21.6 Schematic of the frequency-domain imaging system developed at Dartmouth College. (From Pogue, B.W. et al., *Opt. Express*, 1, 391, 1997. With permission.)

21.3.1.2 Frequency-Domain Imaging System

A typical frequency-domain imaging system is illustrated in Figure 21.6. Developed at Dartmouth College,[215] this system modulates the intensity of a laser diode at 100.000 MHz and couples the light sequentially into different fiber optics (the SS-TDM encoding scheme). Diffusely remitted light is captured by detector fibers that are coupled into a single photomultiplier tube (PMT). The PMT is time-shared between the individual detector fibers, so the instrument employs a TDM encoding scheme. A filter wheel is positioned before the PMT to prevent saturation of the detector by stronger optical signals coming from closer to the source. The photo-electric signal within the PMT is modulated at 100.001 MHz to heterodyne the signal down to 1 kHz. The 1-kHz signal is acquired by an analog-to-digital converter, from which a computer calculates the relative amplitude and phase of the detected 100-MHz diffuse photon density wave.

21.3.1.3 Time-Domain Imaging System

Figure 21.7 shows a diagram of the time-domain image system developed at University College London.[216] The light source is a subpicosecond pulsed Ti:Sapphire laser with wavelength tunable from approximately 750 to 850 nm. Laser pulses are fiber coupled and fiber-optically multiplexed between 32 fibers that deliver source light to 32 independent positions. Photons exiting the sample are received by 32 large diameter detector fibers that relay the light to 32 individual time-correlated single photon counting channels. Computer controlled variable optical attenuators ensure that the detected light intensity does not saturate the photodetectors. The arrival time of detected photons is histogrammed by a picosecond time analyzer, which simultaneously produces histograms of the measured TPSF for all 32 detector channels. The full set of TPSFs for all source-detector pairs represents the raw data used for reconstructing images.

21.4 Experimental Diffuse Optical Tomography: Functional Breast and Brain Imaging

The imaging systems described previously and others like them have been used in phantom, animal, and human subject studies. In this section we provide a coherent snapshot of these activities. We begin with

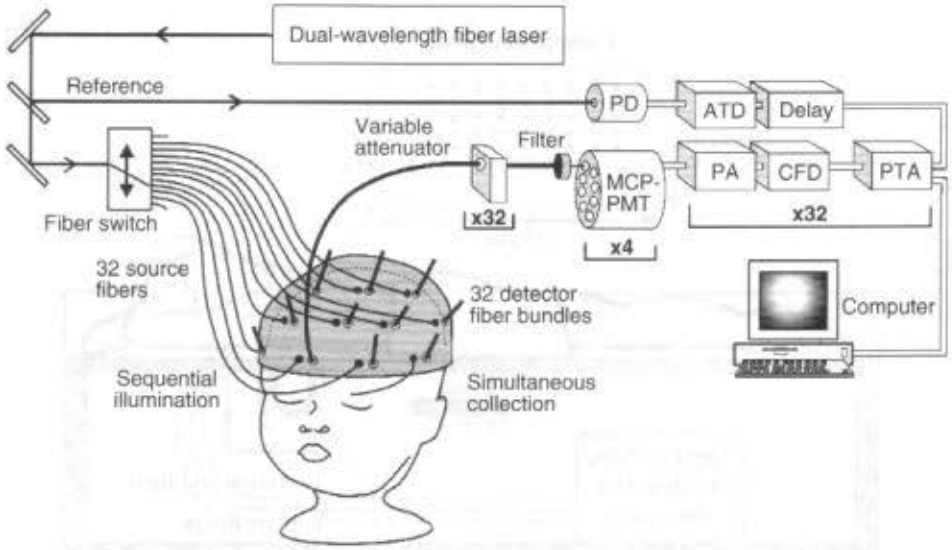

FIGURE 21.7 Schematic diagram of the time-domain imaging system. For clarity, only one detector fiber bundle is shown. PD = photo diode; PA = pre-amplifier; ATD = amplitude timing discriminator; CFD = constant fraction discriminator; PTA = picosecond time analyzer.

a tissue phantom experiment in order to illustrate image reconstruction on a controlled sample; the DOT reconstructions produce acceptable images by striking a balance between image noise, contrast, and resolution. Next we review the application to breast imaging, with recent clinical results. We describe measurements of normal breast optical properties, of tumors based on endogenous contrast, and of tumors using exogenous contrast agents to enhance tumor absorption characteristics preferentially.

Finally, we review the application to functional brain imaging. In this case we show images of blood flow, blood volume, and oxygen saturation changes in a rat stroke model. Then we show images that reveal localized variations in cerebral hemodynamics due to a sensory stimulation of a rat. Finally, we provide an example of functional brain imaging in adult humans with motor-sensory stimuli. The experiments presented are not exhaustive and do not represent the full range of results from the community. Nevertheless, the selected experiments indicate the promise of DOT for *in vivo* functional imaging.

21.4.1 Multiple Absorbers in a Slab Phantom

In this subsection we show how DOT is able to resolve multiple perturbations in the optical properties of a highly scattering medium. We also illustrate the trade-off between image resolution and the contrast-to-noise ratio. This type of experiment is important because it validates DOT techniques in well controlled samples.

The experimental data were collected using a hybrid CW and RF system developed at the University of Pennsylvania[217,218] (see Figure 21.8). Laser light is multiplexed to 45 positions (a 9×5 array) on one side of the slab phantom (i.e., parallel planes, see Figure 21.8). Nine detector fibers are interspersed within the 9×5 array to receive a 70 MHz frequency-domain signal, simultaneously, from which the amplitude and phase is determined by an IQ-homodyne demodulation.[219] This frequency-domain information was used to determine the background optical properties of the medium. A 16-bit CCD camera (Roper Scientific, NTE1340) was positioned to image the CW light transmitted through the phantom. The CCD camera had 800×1120 pixels, which were binned 24×24. The measurements were cropped to within a radius of 6 cm of the maximum transmitted signal producing approximately 250 independent measurements (i.e., a 21×13 detector array) per source position.

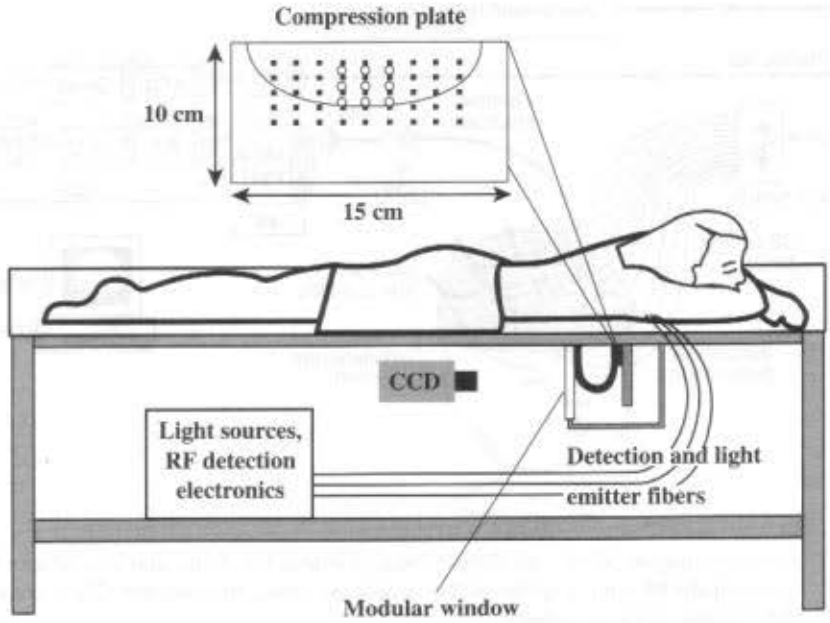

FIGURE 21.8 Phantom geometry for the transillumination measurements. The array of 9 × 5 light sources is indicated in the compression plate by the black squares. The 3 × 3 array of frequency-domain photodetectors intermingled with the source fibers is indicated by the open circles. A CCD camera images the transmission of the CW light from each source position individually. A slightly modified version of this experimental system was used for the clinical measurements described in Section 21.4.1, with the CCD camera replaced by a scanning frequency-domain photodetector.

For the phantom experiment, the breast tank was filled with an Intralipid/ink solution (see Figure 21.8)[220,221] with $\mu_s' = 8\ cm^{-1}$ and $\mu_a = 0.05\ cm^{-1}$. In one experiment, two highly absorbing spheres ($\mu_a = 2\ cm^{-1}$ and $\mu_s' = 8\ cm^{-1}$) were suspended in the Intralipid solution with a 5-cm separation; in another experiment many more spheres were suspended in the Intralipid solution. The image reconstruction algorithm was formulated using the Rytov approximation to the integral solution of the diffusion equation (see Section 21.2.5.2). A finite difference scheme was used to solve the forward problem in the rectangular geometry, and a conjugate gradient method was used to solve the inverse problem. Regularization was used for the inverse problem (see Section 21.2.5.3), and the entire scheme was iterative. Convergence was consistently obtained after 15 iterations.

An image of the two spheres was reconstructed with optimal regularization (see Figure 21.9). The three-dimensional image shows that two absorbers are easily resolved. The optimal regularization parameter was determined by examining the dependence of the regularization parameter on image norm, image variance, full-width at half-maximum (FWHM) of the imaged absorber, and measurement residual (see Figure 21.10). When the numerical value of the regularization parameter was increased, the image norm and image variance decreased, but at the expense of decreased image resolution (i.e., an increase in FWHM of the spheres) and increased measurement residual. A plot of the image contrast-to-noise ratio vs. the regularization parameter indicates that contrast-to-noise ratio is optimized with a regularization parameter that balances image noise and resolution (see arrows in Figure 21.10).[217] Similar trade-offs between image noise and resolution can be expected when imaging animals and human subjects. Culver et al.[217] also demonstrated images of many (i.e., >10) spheres in the same sample volume, thus indicating the potential of DOT for reconstructing multiple heterogeneities (as opposed to isolated heterogeneities in a homogenous background).

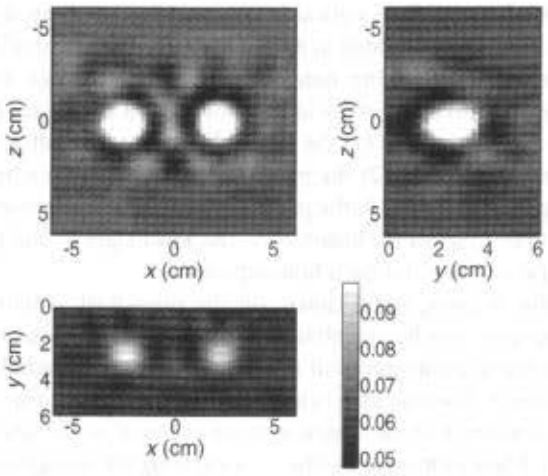

FIGURE 21.9 Three slices of the three-dimensional absorption image reconstructed from the phantom data are shown. The *x*-*z* plane is parallel to the measurement planes of the phantom. The scale bar indicates the range of values for the absorption coefficient.

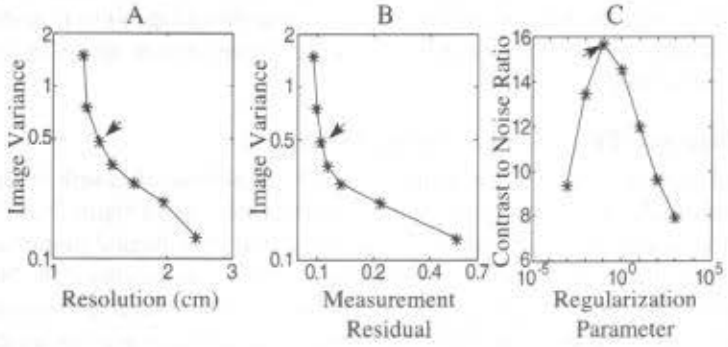

FIGURE 21.10 The dependence of objective measures of image quality on the regularization parameter is shown. (A) Increasing the regularization parameter controls the trade-off between image noise and resolution. (B) Increasing the regularization parameter also increases the residual of the fit to the experimental data. (C) The optimal regularization parameter as determined by the maximum image contrast to noise ratio corresponds to the points in (A) and (B) that balance image noise and resolution/measurement residual (indicated by the arrows in each figure).

21.4.2 Breast Imaging

The use of light to detect tumors in the breast was first proposed by Cutler in 1929,[83] who hoped to be able to distinguish between solid tumors and cysts in the breast by illuminating the breast and shadowing the tumors. However, he found it difficult to produce the necessary light intensity without exposing the patient's skin to extreme heat, while the low resolution of the technique severely limited its clinical applications. With the advent of more modern optical sources and detectors, optical transillumination breast imaging was tried again in the 1970s and 1980s, but was abandoned because of lack of sensitivity and specificity.[93,222,223] The burst of activity in the 1990s can be traced to widespread acceptance of the diffusion approximation, which provides a tractable basis for tomographic approaches to image reconstruction using highly scattered light. Tomographic methods are crucial for recovery of information about heterogeneous breast tissues.

Functional, tomography-based diffuse optical breast imaging has been demonstrated, but further understanding and improvements are needed in order for it to become clinically useful. Current research is focusing on the construction of imaging systems with higher resolution and increased quantitative accuracy, as well as on the improvement of the algorithms used in image reconstruction. Thus far three general patient positions have been used: (1) the patient lies prone on a cot with a breast (or breasts) in a pendant position for imaging;[15,190–192] (2) the patient sits or stands with a breast held in compression similar to x-ray mammography;[10–13] and (3) the patient lies supine and is imaged with a hand-held probe that is moved to different positions on the breast.[119,193] The advantages of one approach over another for extraction of optical properties have not been fully explored.

Current research is also focusing more closely on the physiological information available to the technique. For example, quantitative hemoglobin images of the female breast showed localized increases in hemoglobin concentration that corresponded with biopsy-confirmed pathological abnormalities, suggesting that NIRS is capable of characterizing tumors as small as 0.8 ± 0.1 cm.[15] Other investigators have focused on the intrinsic sensitivity of the optical method to blood, water, and adipose — the principal components of the breast. Many of these researchers are studying the changes in breast optical properties associated with age, exogenous hormone levels, and menopausal status as well as, to a lesser extent, fluctuations in menstrual cycles.[14,224] Still other researchers are exploring the use of contrast agents[13,225,226] and the combination of DOT with other imaging techniques such as MRI and ultrasound.

In this section we briefly review some recent advances in the application of DOT to breast imaging. Our first example establishes the baseline optical properties of the normal breast; such information provides a useful benchmark about the requirements for detection of tumors based on endogenous (and exogenous) contrast. Then we describe experiments that image the endogeneous properties of the breast, revealing tumor signals, and we describe experiments that utilize contrast agents to create images with improved tumor sensitivity.

21.4.2.1 Endogenous Properties of Normal Breast

Our group at the University of Pennsylvania has collected optical breast data with the subject in a prone position, using essentially the same system discussed in Reference 218 (see Figure 21.8). The goal of these measurements was to establish *in-vivo* the baseline optical and physiological properties of the normal breast. The experimental system employed diode lasers at three wavelengths (750, 786, and 830 nm), each modulated at 140 MHz. The source light was delivered to the moveable breast-stabilization plate through an optical fiber. For detection, the CCD camera in Figure 21.8 was not used; instead a fiber-coupled PMT was scanned to multiple positions on the breast with the source fiber fixed at the center of the tissue and scan region. Prior to collecting data, the tank surrounding the breast is filled with a scattering liquid whose optical properties closely approximated the breast tissue. The amplitude and phase of the transmitted DPDW was measured using a homodyne IQ demodulation scheme.[219] In 15 min, 153 measurements (17×9) are obtained over an area of 10 cm $\times$ 7 cm (x,y).

Measurements were collected on 52 healthy volunteers. The analysis had one new innovative feature: the data were fit simultaneously at all three wavelengths and "reconstructed" using spectral responses of oxy- and deoxyhemoglobin, and a Mie-based model for the wavelength dependence of the scattering coefficient. This spectroscopically self-consistent approach reduced crosstalk between scattering and absorption, overcoming some of the limitations of the homogeneous tissue model often used for characterization. The average absorption and scattering coefficients of the normal breast tissue were found to be 0.041 ± 0.025 cm^{-1} and 8.5 ± 2.1 cm^{-1}, respectively, at 786 nm. The mean blood volume and blood oxygen saturation were found to be 34 ± 9 μM and $68 \pm 8\%$, respectively.

A scatter plot of the blood volume and blood saturation results is shown in Figure 21.11. We see from this plot that the optical method will be sensitive to tumors with large blood volume and low blood saturation (outside the dashed lines); this condition might prevail in many tumors. A weak correlation of total hemoglobin concentration and scattering with body mass index (BMI) was found (i.e., decreasing with increasing BMI), but no statistically significant correlation with age was observed (20 to 65 years). This information provides insight into the types of intrinsic contrast available to optical breast imaging

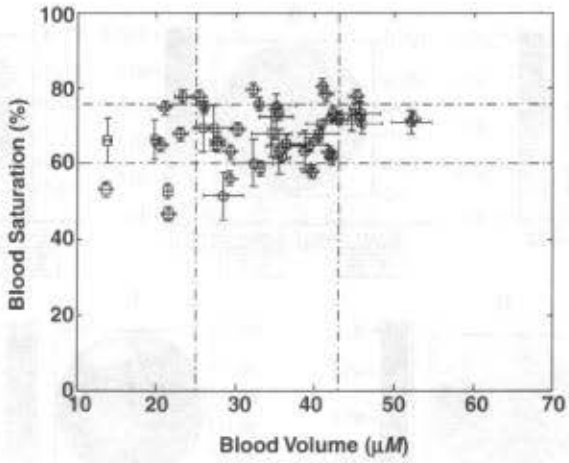

FIGURE 21.11 Hemoglobin saturation vs. total hemoglobin concentration; the dashed lines indicate the ranges for normal tissue from the mean and standard deviation of the healthy breast tissue.

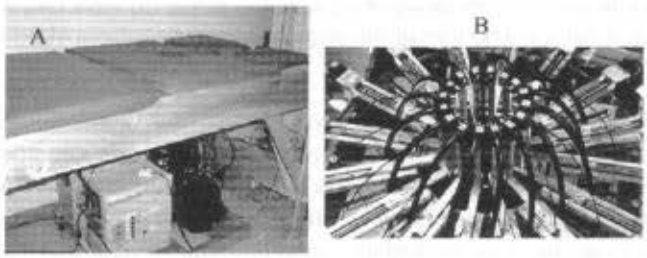

FIGURE 21.12 (A) Patient bed for the optical breast imaging system developed at Dartmouth. (B) The fiber optic array for coupling light to and from the patient. The larger black cables are the detector fibers. The fibers are mounted on posts that translate radially for making contact with the tissue.

and, importantly, indicates the range of values that malignant tumors must have to be clearly distinguishable from the typical variation of normal breast tissue.

21.4.2.2 Clinical Optical Images of Breast Lesions

The optical breast imaging system developed by the group at Dartmouth is shown in Figure 21.12.[15,191] It is a pendant system, similar in many respects to the one at the University of Pennsylvania, but it obtains a coronal image of one breast at a time with a ring of interspersed 16 source and 16 detector fibers. The fiber ring is vertically positioned by a translation stage to image different planes of interest. The laser diodes emit light at 761, 785, 808, and 826 nm, are modulated at 100 MHz, and are optically combined before being serially multiplexed to each of the 16 source fibers. The lasers are driven sequentially so that the signal at each of the 16 photodetectors distinguishes different wavelengths and positions by time-division multiplexing. At each of the 4 wavelengths, 256 independent measurements are obtained and then processed by a finite element program to reconstruct absorption and scattering images (as described in Pogue et al.[15] and McBride et al.[191]).

Figure 21.13 shows optical images for a 73-year-old female volunteer who had undergone routine mammography that demonstrated a 2.5-cm focal density with a larger ~6-cm-diameter area of associated architectural distortion. The imaged lesion corresponded to a palpable mass; needle biopsy subsequently diagnosed the mass as an invasive ductal carcinoma. The optical image was acquired 2 weeks after the biopsy and was aligned such that the coronal imaging plane was centered on the palpable lump. From

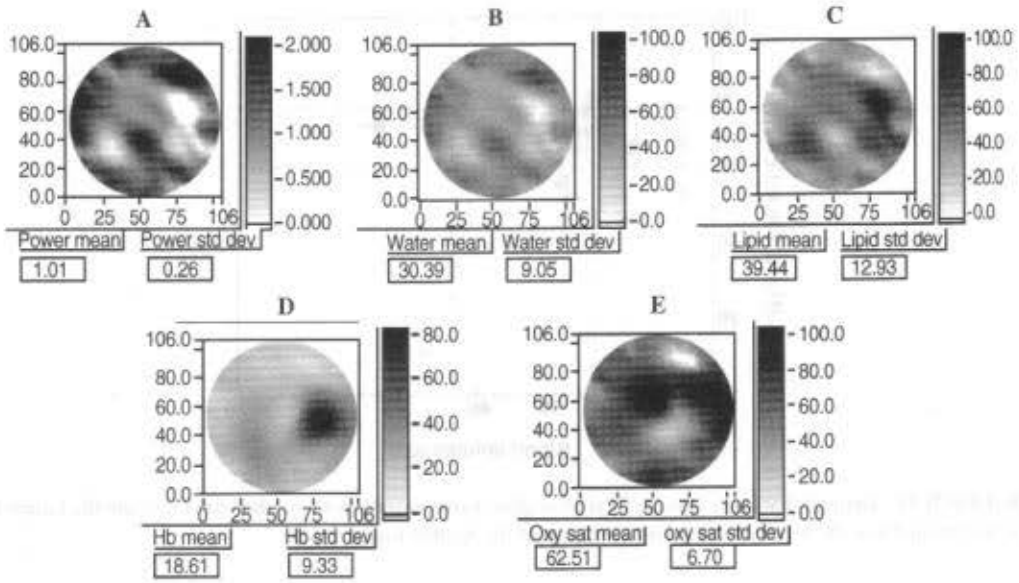

FIGURE 21.13 Clinical breast images are shown of (A) scattering power, (B) water (%), (C) lipids (%), (D) total hemoglobin concentration (μM), and (E) hemoglobin oxygen saturation (%). (From McBride, T.O. et al., *J. Biomed. Opt.*, 7, 72, 2002. With permission.)

the scattering and absorption information, images were derived of the scatter power,[191,227] water concentration, lipid concentration, total hemoglobin concentration, and oxygen saturation. A lesion is clearly visible in the total hemoglobin image, which shows a threefold contrast-to-background ratio. In comparison to the variation of total hemoglobin concentration observed in normal tissue (Figure 21.11), the tumor has significantly greater total hemoglobin concentration. Structures in the other physiological images do not correspond well to the hemoglobin image; however, sensitivity to water and lipid percentages is expected to be weak because of the chosen wavelengths. The similarity between the scattering power, water, and lipid images suggests that water and lipid images are susceptible to crosstalk from the scattering power image.

21.4.2.3 Contrast Agents to Enhance Breast Lesion Detection

Another experiment at the University of Pennsylvania employed a time-domain imaging system in transmission mode to acquire *contrast enhanced* breast images while simultaneously obtaining magnetic resonance images. The time-domain optical imager has been described in detail in References 13 and 228. The instrument uses time-correlated single photon counting to measure the TPSF of photons diffusing through the breast tissue. The TPSF is then Fourier transformed to produce data at multiple modulation frequencies, which are then used to reconstruct differential absorption images[188] of the contrast agent ICG. The 830-nm pulsed laser source is coupled to 24 source fibers through a fiber optic switch. The detection collects light from eight positions simultaneously. Thus images are obtained using 24×8 measurements times the number of modulation frequencies. All source fibers are mounted on one plate forming a 3×8 array of fibers spaced by intervals of 1.25 cm. The detector fibers are mounted on the other plate to form a 2×4 array with a 2.5-cm separation. These two plates stabilize the breast and also contain the RF coils for the MRI. The MR studies were performed with a 1.5 T Signa, GE Medical Systems imager.

Figure 21.14 shows the results from a 70-year-old patient with an infiltrating ductal carcinoma about 1 cm in diameter. The pre-gadolinium (Gd) enhanced sagittal MR image slice passing through the carcinoma is shown in Figure 21.14A in gray scale, while the relative signal increase due to the Gd is

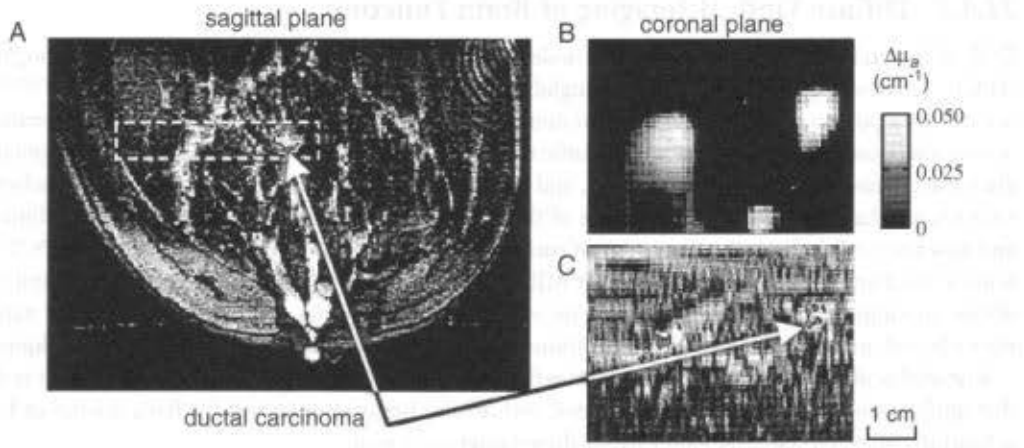

FIGURE 21.14 **(Color figure follows p. 28-30.)** A dynamic MRI and contrast-enhanced DOT image of a ductal carcinoma. (A) A dynamic sagittal MR image after Gd contrast enhancement passing through the center of the malignant lesion. (B) The coronal DOT image, perpendicular to the plane of the MRI image in (A), but in the volume of interest indicated in (A) by the dashed-line box. (C) The dynamic MR coronal image resliced from the same volume of interest and same dimensions as (B).

shown in color. A rectangle surrounding the carcinoma indicates the sagittal cut of the region of interest that was reconstructed in the optical image (shown in Figure 21.14B) in the coronal plane, and the corresponding MR coronal slice shown in Figure 21.14C. A strong optical contrast-induced absorption increase is seen in the upper right of the optical image, congruent with the position of the carcinoma revealed in the coronal MR image. Another lesion is revealed in the left of the optical image, congruent with the Gd enhancement observed in the MR image, but with a different size and shape. The differences in size and shape can be explained by the low spatial resolution of this implementation of DOT and the chosen threshold level for displaying the images. Similar results were seen in other patients with malignant and benign lesions. A summary of tissue ICG absorption enhancement seen in a group of patients is shown in Figure 21.15. This summary suggests that malignant lesions enhance absorption more than benign lesions by a factor of two, and more than normal tissue by a factor of three to four.

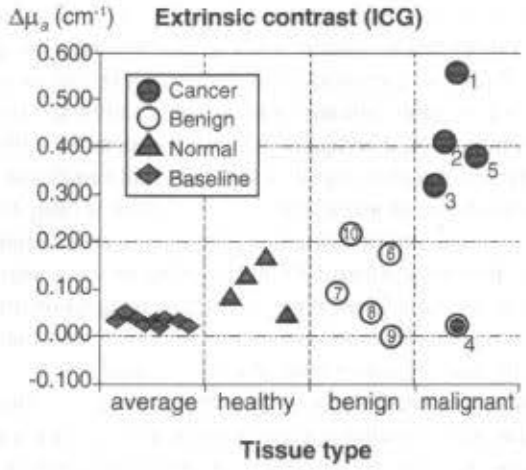

FIGURE 21.15 The ICG-induced absorption enhancement in healthy tissue and benign and malignant lesions compared with the nonenhanced absorption coefficient of normal healthy tissue.

21.4.3 Diffuse Optical Imaging of Brain Function

DOT of the brain affords continuous, *in vivo* deep tissue[161,229] measurements of cerebral oxyhemoglobin (HbO), deoxyhemoglobin (Hb), total hemoglobin (HbT = HbO + Hb), and even blood flow.[197,230–232] It is therefore a potentially new and important noninvasive technique for bedside monitoring. For example, optical spectroscopy can provide crucial information about cerebral hemodynamics and oxygenation during acute and chronic brain conditions, and optical imaging enables the detection of brain ischemia, necrosis, and hemorrhage.[233,234] Knowledge of the most appropriate optical parameters to use clinically, and how they reflect the pathophysiology of such conditions, is still evolving. It is unlikely that DOT will achieve the anatomical resolution of CT or MRI, but its noninvasive nature, low cost, and capability to obtain continuous, real-time information on cerebral hemodynamics and oxygenation under various physiological and pathophysiological conditions constitute a major advantage over other techniques.

Knowledge about how optical parameters reflect tissue pathophysiology is still evolving, but it is clear that application areas for DOT are associated with stroke, brain trauma, and the basic science of brain activation. We elaborate briefly on each of these target areas next.

Diffuse optical tomography offers an attractive alternative for diagnosing and monitoring internal bleeding and ischemic stroke when CT and MRI are not available. There are several possible optical signal indications of stroke. Using a bolus of intravascular contrast agent, it is possible to monitor mean cortical transit times; transit time changes there can reveal flow variations associated with ischemic stroke. Quantitative differential spectroscopy can indicate alterations in hemoglobin saturation in affected tissue due to reduced perfusion or modulated metabolic demand. Bleeding stroke can also be detected spectroscopically, in this case via a large blood volume increase. Scattering contrasts are also possible. Edema and swelling may provide heterogeneities in images of tissue scattering.

The feasibility of near-infrared spectroscopy (NIRS) to detect brain hemorrhage in patients with head trauma has been demonstrated.[27] Studies that compare primitive diffuse optical measurements of brain hematomas with CT images clearly demonstrate a correlation between the optical signal and hematoma location.[26,27,235] These correlation studies have shown that subcortical hemorrhages as deep as 3 cm beneath the cortical surface and as small as 5 mm in diameter can be detected. Furthermore, the different classes of hemorrhages give characteristically different signals. These pilot NIRS results are promising, but they are based on simple relative NIRS measures. Quantitative images of hemoglobin saturation and fast hemodynamics will provide great improvement in available diagnostic information over the data involved in these pilot studies. A means to detect early hemorrhage in at-risk patients — i.e., those treated with thrombolysis or anticoagulants — would have tremendous value. In addition, swelling and edema may be detectable through alterations in the scattering coefficient of the tissue.

Beyond the clinical uses described previously, DOT is experiencing widespread application in functional brain imaging. Since the first demonstrations of noninvasive optical measures of brain function,[29–31] studies have been performed on adult humans using visual,[32] auditory,[33] and somatosensory stimuli.[34] In addition, a number of studies have investigated the motor system.[35–37] Other areas of scientific investigation have included language,[38] higher cognitive function, and functional studies of patient populations.[39–41] Following in the footsteps of functional MRI,[236,237] DOT is likely to play an important role in increasing our knowledge of brain activity associated with various stimulation paradigms, as well as our understanding of cerebral physiology, particularly the coupling between neuronal activity and the associated metabolic and vascular response. Interestingly, optical imaging is potentially the only neuroimaging modality that can measure the hemodynamic (see references above) and metabolic response[238–244] associated with neuronal activity, and measure neuronal activity directly.[245–247]

In the remainder of this section we describe three recent experiments. The first experiments measure flow, hemoglobin saturation, and hemoglobin concentration in a rat during stroke; this combination of parameters ultimately makes possible the assigment of oxygen metabolism changes to specific tissue volumes. The second and third sets of experiments image functional activation in the rat and in humans, with high spatial and temporal resolution.

21.4.3.1 Flow and Blood Oxygen Saturation Images of Rat Stroke

Experimenters at the University of Pennsylvania have used DOT to examine the spatial–temporal evolution of focal ischemia in a rat model.[248] Their measurements probe through the *intact* rat skull and combine "static" diffuse photon density wave measurements of Hb and HbO concentrations with "dynamic" diffuse correlation flowmetry (see Section 21.2.6). Their results are the first application of DOT correlation flowmetry to experimental stroke models.

Figure 21.16A shows the TTC stain of the infarct region of a focal ischemia induced in the rats by intraluminal suture occlusion of the middle cerebral artery. After 60 min of occlusion the suture was retracted for reperfusion. The animals recovered and, at 24 h after occlusion, were sacrificed for TTC staining. Differential images of the concentrations were reconstructed in a slice at a depth of 2 mm below the skull surface, extending 5 mm either side of midline and from 2 mm anterior of bregma to 8 mm posterior of bregma. The hemoglobin and flow images were obtained using the linear Rytov approach described in Sections 21.2.5.2 and 21.2.5.3.

Figure 21.16B shows image slices of total hemoglobin concentration ([HbT]), blood oxygen saturation StO_2, and relative changes in cerebral blood flow (rCBF) reconstructed with DOT. Note that the measurements cover the predominantly penumbral tissue and an equivalent tissue volume on the contralateral side. Image stacks were reconstructed from measurements averaged over five animals. Images are shown for time points representing baseline (–8 min), occlusion (+30 min), and reperfusion (+80 min). Regions of interest (ROIs) were defined for the contralateral and ipsilateral sides, consisting of 4 × 8 mm areas centered in the respective half of each image; the time traces for [Hb], StO_2, and (rCBF) in these regions are plotted in Figure 21.16C. Occlusion and saturation decreased by about 40% from baseline in the affected hemisphere. The numbers for flow are in reasonable agreement with near-surface laser Doppler measurements of penumbral tissues. The cerebral blood volume, on the other hand, showed much smaller percentage changes during occlusion.

These images demonstrate the feasibility of continuously imaging an integrated set of hemodynamic parameters through the time course of ischemia and reperfusion in experimental focal ischemia models. The combined measurements also offer the possibility to make quantitative maps of differential oxygen metabolism. A simplified model for oxygen metabolism relates two of the measurements made. If we assume that the product of the blood perfusion rate with the difference in oxyhemoglobin concentration between the artery perfusing the tissue and the vein draining the tissue equals the oxygen consumption rate, then the measured changes enable us to construct a map of local variations in cerebral oxygen metabolism in deep tissues.[197] This exciting prospect further enhances the attractiveness of the diffuse optical method.

21.4.3.2 Activation Imaging of Brain Function in a Rat Model

In this section we describe applications to functional activation of the rat brain. By using classical functional stimulation paradigms, these studies provide an opportunity to evaluate the imaging capabilities of diffuse optical tomography through comparisons with exposed cortex and fMRI studies.

These studies employed the CW system developed at the MGH-NMR center (see Section 21.3.1.1). The dual wavelength sources were positioned on a 3 × 3 grid interspersed within the 4 × 4 grid of detectors. In accordance with standard procedures used in exposed cortex studies of functional activation, the baseline hemoglobin concentrations were assumed — i.e., [Hb] = [HbO] = 50 μM.[249] Absorption coefficients were calculated using published spectra. The scattering coefficient was assumed to be equal to 10.0 cm^{-1}.

The experiments were performed on adult male Sprague-Dawley rats weighing 300 to 325 g. The rats were fasted overnight before measurements. The animals were anesthetized (Halothane 1 to 1.5%, N_2O 70%, O_2 30%) and catheters were placed into a femoral artery to monitor the arterial blood pressure and into a femoral vein for drug delivery. The animals were tracheotomized, mechanically ventilated, and fixed on a stereotaxic frame. The probe was then placed symmetrically about midline. It covered a region from 2 mm anterior to 6 mm posterior of the rhinal fissure. After the surgical procedures,

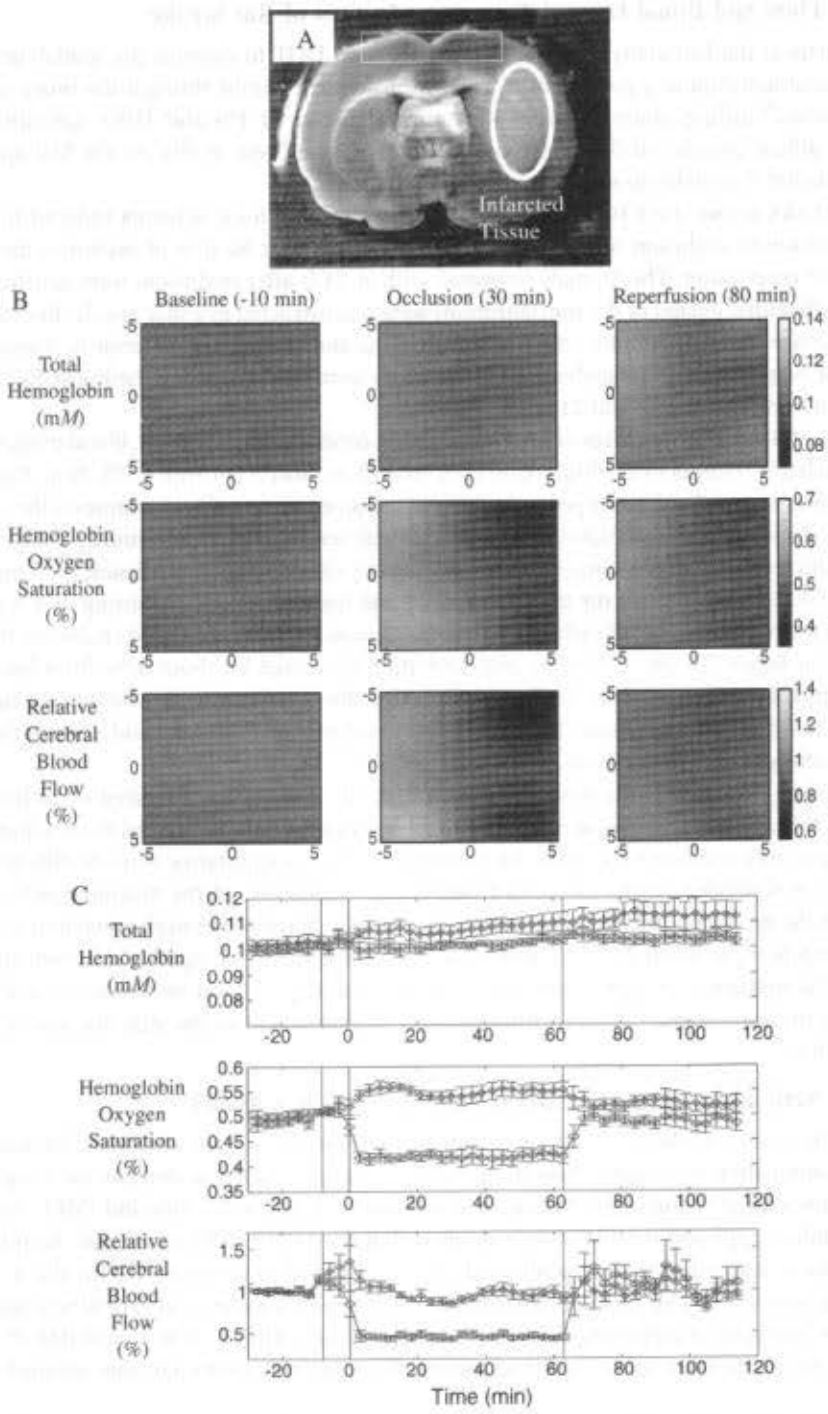

FIGURE 21.16 (A) TTC staining of infarct area; rectangle indicates slice position of DOT image reconstruction. (B–C) Diffuse optical tomography images of total hemoglobin concentrations, tissue averaged hemoglobin saturation, and relative cerebral blood flow (rCBF). A middle cerebral artery occlusion was performed during the time from $t = -5$ min to $t = 0$. The suture was retracted at $t = 60$ min resulting in reperfusion. (B) Images at baseline, during occlusion (+30 min) and +80 min. The spatial dimensions are given in millimeters. The scale bars indicate the concentration of hemoglobin, the percent oxygen saturation, and the relative blood flow change where 1 is no change and 1.4 is a 40% change. (C) The time traces for ipsilateral and contralateral ROIs.

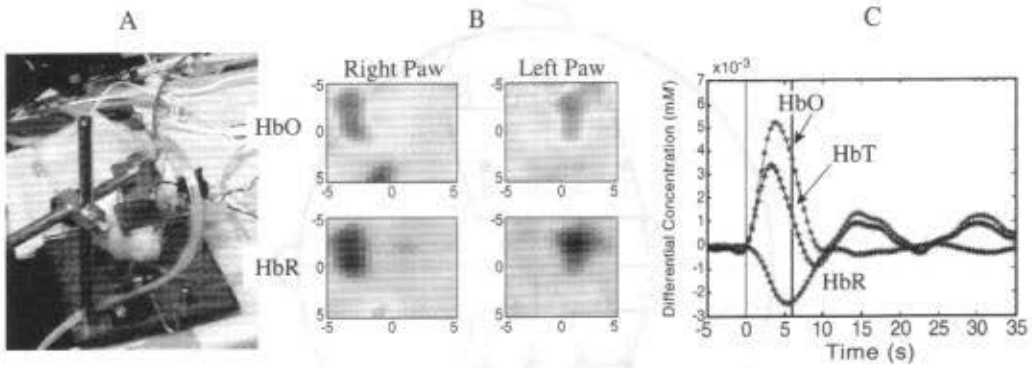

FIGURE 21.17 (A) Photograph of the DOT fibers on the rat scalp. (B) DOT images of oxy- and deoxyhemoglobin concentrations during functional activation of the somatosensory cortex. The oxyhemoglobin (HbO) images exhibit a concentration increase. The deoxyhemoglobin (HbR) images exhibit a concentration decrease. Images are shown for left- and right-forepaw stimulation, the activation showing up on the contralateral side. (C) Time-course of the hemoglobin concentration changes in the region of interest defined by the significant focal concentration change seen in (B).

Halothane was discontinued, and anesthesia was maintained with a 50 mg/kg intravenous bolus of α-chloralose followed by continuous intravenous infusion at 40 mg/kg/hr.

Electrical forepaw stimulation was performed using two subdermal needle electrodes inserted into the dorsal forepaw. The stimulus pattern was relayed to an isolated, pulsed current supply to provide 300 μ_s constant current pulses at programmed times. The current was maintained at 1.0 mA. A 3 Hz, 6-s stimulus was provided with 54-s interstimulus interval. The measurements were then averaged over 42 stimulus intervals. The final averaged temporal data stack was reconstructed frame by frame using the methods described in Sections 21.2.5.2 and 21.2.5.3. Each slice was reconstructed at a depth of 2 mm from the skull surface extending 5 mm either side of midline, and from 2 mm anterior of bregma to 8 mm posterior of bregma. The absorption image stacks were then converted to oxy- and deoxyhemoglobin image stacks.

The series of DOT [Hb] and [HbO] images show focal activation contralateral to the stimulated forepaw. The images are frames taken every 5 s. The time traces were extracted for a 3 × 3 mm area centered at maximal activation (see Figure 21.17). The oscillations seen after stimulus are similar to vasomotion signals seen by optical studies in exposed cortex.[250]

21.4.3.3 Images of Brain Function in Humans

The same MGH CW imaging system described in Section 21.3.2.1 was used to study 15 subjects during finger tapping, finger tactile stimulation, and median nerve electrical stimulation. The finger tapping and finger tactile protocols consisted of series of 10 stimulation/rest sequences for each hand (i.e., 20-s stimulation and 20-s rest), wherein the stimulation occurs at a frequency of ~4 to 5 Hz (the stimulus frequency of each subject was adjusted so as to be anharmonic with the heart rate). The median nerve electrical stimulation protocol consisted of a series of 18 stimulation/rest sequences (i.e., 10-s stimulation and 20-s rest) with stimulus intensity slightly above the motor threshold (i.e., using rectangular electrical pulses, current peak: <10 mA, duration: 0.2 ms, repetition rate: 4 to 5 Hz). Motion sensors were used on the fingers of the subjects to synchronize the stimuli with the optical signals recorded on the head.

The optical data were band-pass filtered between 0.02 to 0.50 Hz to correct for slow drifts and to reduce the ~1-Hz arterial pulsation amplitude. Finally, the multiple stimulation sequences were block averaged to achieve better statistics. This resulted in a time series of the measured signal intensity for each source-detector pair. Source-detector pairs near a region of brain activation showed changes similar to those seen in a rat as shown in Figure 21.18, while the other source-detector pairs showed little signal variation. Absorption images at the different wavelengths were converted into images of changes in oxy- and deoxyhemoglobin concentrations.

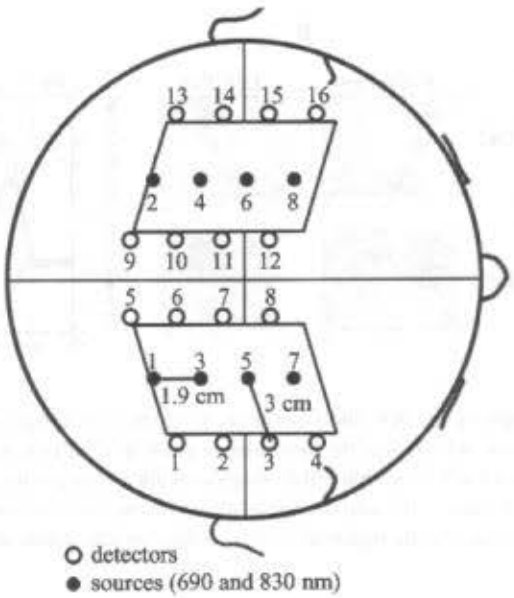

FIGURE 21.18 Geometrical arrangement of source and detector fibers on the head.

The hemodynamic response to stimulation was always visible in the optical data. During the finger tapping experiment, the oxy- and deoxyhemoglobin concentration variations were not sharply localized. This is probably because of a systemic elevation in blood volume, presumably resulting from a corresponding heart rate increase. During finger tactile stimulation, oxyhemoglobin increases were two to three times smaller than during finger tapping; also, oxy- and deoxyhemoglobin were sharply localized. During electrical stimulation, the hemoglobin changes were sharply localized and had a magnitude comparable with finger tactile stimulation. In the latter experiments a peculiar feature of ipsilateral decrease in blood volume was observed during the stimulation period (see Figure 21.19). By contrast, magnetoencephalography (MEG) and functional magnetic resonance imaging (fMRI) studies during median nerve stimulation have shown an activation of only the contralateral primary sensory-motor cortex.[251,252] A deactivation of the ipsilateral primary sensory-motor cortex has been observed in previous fMRI experiments during finger tapping;[253] these optical results suggest that a similar decrease in blood flow occurs in the ipsilateral cortex during electrical somatosensory stimulation.

In summary, DOT offers an exciting new method for studying human brain function, and should play an important role in the brain sciences when other imaging modalities (e.g., fMRI, EEG, MEG) are not attractive because of cost, sensitivity to motion artifacts, or confinement of the research subject.

21.5 Fundamental and Practical Issues: Problems and Solutions

In this final section we touch on some of the fundamental and practical difficulties associated with DOT. In particular, we discuss the fundamental limits of detection, characterization, and resolution, we discuss practical problems of source-detector calibration, and we briefly outline some of the ways researchers are overcoming these barriers.

21.5.1 Detection, Localization, Characterization, and Resolution Limits

The detection limits of DOT are set by the smallest signal perturbation that can be detected above the noise level. The spatial localization limit is generally the same as the detection limit because the maximum signal perturbation often occurs when an object is located directly between a source and detector. Full characterization of object optical properties, shape, size, and position is more difficult than detection and

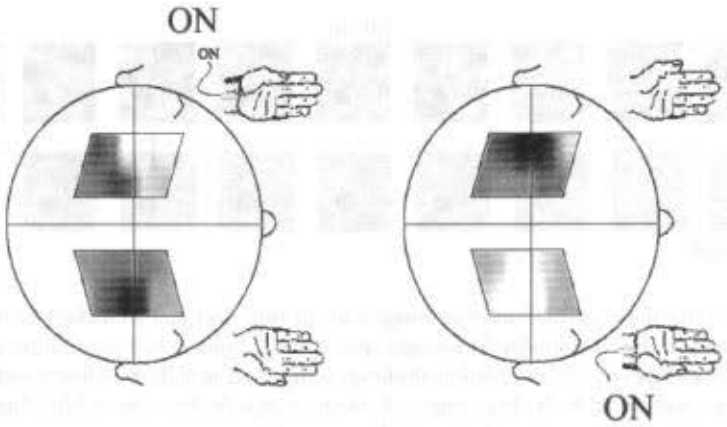

FIGURE 21.19 Block average hemoglobin maps at the end of the electrical stimulation period. Top panels: deoxyhemoglobin changes; bottom panels: oxyhemoglobin changes. Left panels: left wrist median nerve stimulation; right panels: right wrist median nerve stimulation.

localization. For example, a fixed signal perturbation can be caused by a small, strongly absorbing object or a large, weakly absorbing object. The distinction between the large and small object must be derived from relative spatial differences in the perturbation of the measured fluence.

These limits have been extensively explored[254] for a transmission geometry applicable to breast imaging. In this work, a best-case scenario noise model assumed shot noise and small positional uncertainties gave rise to a random noise on the order of 0.1% of the signal intensity. Measurements were simulated in the transmission geometry with a single modulation frequency. With these assumptions about the noise, it was possible to detect 3-mm-diameter-absorbing objects that possessed a threefold greater absorption than the background. A similar analysis of the characterization limits indicated that simultaneous determination of object diameter and absorption coefficient required that object diameters were a minimum of 8 to 10 mm (for a 100% contrast); see Reference 254 for details. Another investigation,[255] focusing on resolution (defined as the FWHM of the fluence point-spread function caused by a localized perturbation,[255–257]) found that, if proper deconvolution of the measured data is performed, then resolutions of order 5 to 7 mm are possible with DOT.

There are potentially many ways to overcome some of these barriers, and many researchers are exploring the following possibilities, as well as other ideas. The brute force approach is to increase the number of measurements or decrease the measurement noise. This can be done, by increasing numbers of source-detector pairs, modulation frequencies, or optical wavelengths. The use of many optical wavelengths is beneficial because relatively few significant chromophores are in tissue and their spectra are well known. The use of prior spatial information, for example, the assignment of particular tissue types to specific volume elements of the image,[106,137,258] enables one to reduce the number of unknowns in the inverse problem and thus can effectively improve images. Optical techniques can also be combined with other imaging modalities (e.g., ultrasound[119,137,259] or MRI[13,260,261]) to constrain the DOT problem. Singular-value analysis of the tomographic weight matrix associated with specific data types, geometries, and optode arrangements has been developed recently[123] and should provide experimenters with quantitative tools to optimize for the spatial sampling interval, field-of-view parameters, resolution trade-offs, and, ultimately, physiology. Finally, it is now possible to reduce the systematic errors associated with source-detector amplitudes by directly incorporating these unknowns into the image reconstruction problem. This is the subject of the last section of this chapter.

21.5.2 Calibration of Source and Detector Amplitudes

The modeling of the DOT forward problem requires accurate knowledge of source and detector amplitudes and their positions. Systematic errors in the calibration of these parameters will result in absorption

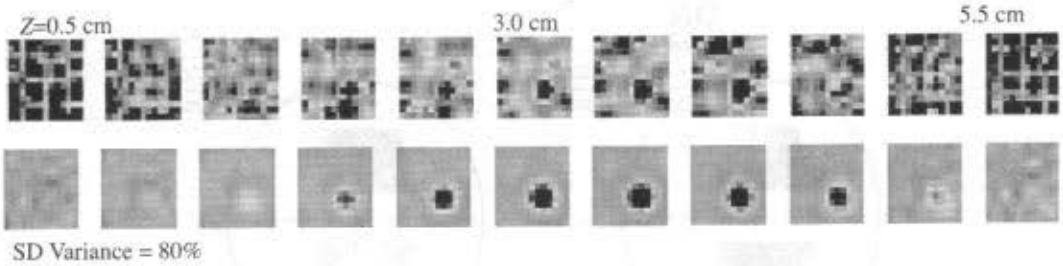

FIGURE 21.20 A three-dimensional absorption image without (top row) and with (bottom row) modeling the unknown source and detector amplitudes. The images span X and Y from –3 to 3 cm; Z-slices are indicated from 0.5 to 5.5 cm. The absorbing object is observable in the image with modeling of the 80% source and detector variance; however, its contrast is obscured by the large amplitude variation near the boundaries. Modeling for the unknown variance provides an image with significantly improved image quality.

and scattering image artifacts, e.g., image spikes near the positions of the sources and detectors. This type of artifact has been observed by a number of groups.[262] Some schemes to minimize these artifacts include median filtering[263] and spatial regularization; the latter approach penalizes the reconstruction near sources and detectors with a weight that varies exponentially from the sample surfaces.[113,262,264] The result is an image with suppressed variations near the sources and detectors, but with improved image quality further from the boundaries. However, the scheme has the undesirable effect of biasing the reconstruction away from the boundaries of the medium.

A recent and relatively simple solution to this problem models the uncertainties of source and detector amplitude and includes them in the inverse problem.[265] Within the linear Rytov approximation, the unknown source and detector amplitudes can be solved simultaneously with the unknown optical properties of the medium. We briefly outline this procedure next, assuming for simplicity a sample with absorption heterogeneities, but without scattering heterogeneities.

Recall the linear approximation for calculating fluence perturbations from spatial variation in the absorption and scattering coefficients, discussed in Section 21.2.5.2. The problem was written in the form $[W]\{x\} = \{b\}$ where $[W]$ represented the weight matrix, $\{x\}$ represented the unknown optical properties, and $\{b\}$ represented the difference between experiment and calculation (or the scattered wave). If we include the unknown source and detector amplitudes into the model, then the matrix equation can be reformulated as $[B]\{\xi\} = \{b\}$ where $[B] = [W' S D]$ and

$$\left\{\frac{\xi}{\varsigma}\right\} = \left\{\frac{\delta\mu_{a,1}}{\mu_{ao}} \cdots \frac{\delta\mu_{a,NV}}{\mu_{ao}} \ln s_1 \cdots \ln s_{NS} \ \ln d_1 \cdots \ln d_{ND}\right\}. \tag{21.22}$$

Here s_i and d_i represent the amplitude of the ith source and detector, respectively, NV is the number of voxels, NS is the number of sources, and ND is the number of detectors. Scaling $\delta\mu_{a,j}$ by μ_{ao} makes the elements dimensionless and of the same order as $\ln s$ and $\ln d$. $\mathbf{W}' = \mu_{ao}\mathbf{W}$ is the rescaling of the standard weight matrix. **S** and **D** are simple, well-defined matrices with block diagonal form that have 1 or 0 in the elements corresponding to particular sources and detectors.

Simulation results have demonstrated that incorporation of the unknown source and detector amplitudes into the inverse problem maintains image quality despite amplitude uncertainties greater than 50%. This is illustrated in Figure 21.20; a simulation of transmission through a 6-cm slab was considered with background optical properties of $\mu_{so}' = 10\ \text{cm}^{-1}$ and $\mu_{ao} = 0.05\ \text{cm}^{-1}$ and a 1.6-cm diameter absorbing sphere with $\mu_a = 0.15\ \text{cm}^{-1}$, centered at $(x,y,z) = (1,1,3)$ cm. Measurements were made with 16 sources and 16 detectors equally spaced from –3 to 3 cm, and continuous-wave measurements were simulated. There was no additive measurement noise (i.e., shot or detector electronic noise) in the simulated data, only the multiplicative model error associated with the source and detector amplitudes.

Acknowledgments

We have benefited from discussions with many colleagues and collaborators and many of their observations are found in this chapter. In particular, we thank Joe Culver, Maria Angela Franceschini, and Gary Boas for significant assistance in the preparation of this chapter. We also thank Turgut Durduran, Jeremy Hebden, Vasilis Ntziachristos, and Brian Pogue for discussion and for providing figures for the chapter. For other useful discussions over many years we thank Simon Arridge, Britton Chance, Regine Choe, Alper Corlu, Anders Dale, Joel Greenberg, Monica Holboke, Xingde Li, Eric Miller, Bruce Tromberg, Guoqiang Yu, and Tim Zhu.

D.A.B. acknowledges funding from Advanced Research Technologies, from National Institutes of Health grants R29-NS38842 and P41-RR14075, from the Center for Innovative Minimally Invasive Therapies, and from the U.S. Army under Cooperative Agreement DAMD17-99-2-9001. The material presented does not necessarily reflect the position or the policy of the government, and no official endorsement should be inferred. A.G.Y. acknowledges partial support from NIH grants 2-R01-CA-75124-04 and 2-RO1-HL-57835-04.

References

1. Yodh, A. and Chance, B., Spectroscopy and imaging with diffusing light, *Phys. Today*, 48, 34, 1995.
2. Tromberg, B., Yodh, A., Sevick, E., and Pine, D., Diffusing photons in turbid media: introduction to the feature, *Appl. Opt.*, 36, 9, 1997.
3. Yodh, A., Tromberg, B., Sevick-Muraca, E., and Pine, D., Diffusing photons in turbid media, *J. Opt. Soc. Am. A*, 14, 136, 1997.
4. Boas, D.A., Brooks, D.H., Miller, E.L., DiMarzio, C.A., Kilmer, M., Gaudette, R.J., and Zhang, Q., Imaging the body with diffuse optical tomography, *IEEE Signal Process. Mag.*, 18, 57, 2001.
5. Miller, E., Focus issue: diffuse optical tomography — introduction, *Opt. Express*, 7, 461, 2000.
6. Chance, B., Near-infrared images using continuous, phase-modulated, and pulsed light with quantitation of blood and blood oxygenation, *Ann. N.Y. Acad. Sci.*, 838, 19, 1998.
7. Kang, K.A., Chance, B., Zhao, S., Srinivasan, S., Patterson, E., and Trouping, R., Breast tumor characterization using near-infrared spectroscopy, *Proc. SPIE*, 1888, 1993.
8. Suzuki, K., Yamashita, Y., Ohta, K., and Chance, B., Quantitative measurement of optical-parameters in the breast using time-resolved spectroscopy — phantom and preliminary *in-vivo* results, *Invest. Radiol.*, 29, 410, 1994.
9. Fishkin, J.B., Coquoz, O., Anderson, E.R., Brenner, M., and Tromberg, B., Frequency-domain photon migration measurements of normal and malignant tissue optical properties in a human subject, *Appl. Opt.*, 36, 10, 1997.
10. Grosenick, D., Wabnitz, H., Rinneberg, H.H., Moesta, K.T., and Schlag, P.M., Development of a time-domain optical mammograph and first *in vivo* applications, *Appl. Opt.*, 38, 2927, 1999.
11. Franceschini, M.A., Moesta, K.T., Fantini, S., Gaida, G., Gratton, E., Jess, H., Mantulin, W.W., Seeber, M., Schlag, P.M., and Kaschke, M., Frequency-domain techniques enhance optical mammography: initial clinical results, *Proc. Natl. Acad. Sci. U.S.A.*, 94, 6468, 1997.
12. Nioka, S., Miwa, M., Orel, S., Shnall, M., Haida, M., Zhao, S., and Chance, B., Optical imaging of human breast cancer, *Adv. Exp. Med. Biol.*, 361, 171, 1994.
13. Ntziachristos, V., Yodh, A.G., Schnall, M., and Chance, B., Concurrent MRI and diffuse optical tomography of breast after indocyanine green enhancement, *Proc. Natl. Acad. Sci. U.S.A.*, 97, 2767, 2000.
14. Cerussi, A.E., Berger, A.J., Bevilacqua, F., Shah, N., Jakubowski, D., Butler, J., Holcombe, R.F., and Tromberg, B.J., Sources of absorption and scattering contrast for near-infrared optical mammography, *Acad. Radiol.*, 8, 211, 2001.
15. Pogue, B.W., Poplack, S.P., McBride, T.O., Wells, W.A., Osterman, K.S., Osterberg, U.L., and Paulsen, K.D., Quantitative hemoglobin tomography with diffuse near-infrared spectroscopy: pilot results in the breast, *Radiology*, 218, 261, 2001.

16. McBride, T.O., Pogue, B.W., Gerety, E.D., Poplack, S.B., Osterberg, U.L., and Paulsen, K.D., Spectroscopic diffuse optical tomography for the quantitative assessment of hemoglobin concentration and oxygen saturation in breast tissue, *Appl. Opt.*, 38, 5480, 1999.
17. Delpy, D.T. and Cope, M., Quantification in tissue near-infrared spectroscopy, *Philos. Trans. R. Soc. London B*, 352, 649, 1997.
18. Painchaud, Y., Mailloux, A., Harvey, E., Verreault, S., Frechette, J., Gilbert, C., Vernon, M.L., and Beaudry, P., Multi-port time-domain laser mammography: results on solid phantom and volunteers, *Int. Symp. Biomed. Opt.*, 3597, 548, 1999.
19. Tromberg, B., Coquoz, O., Fishkin, J., Pham, T., Anderson, E.R., Butler, J., Cahn, M., Gross, J.D., Venugopalan, V., and Pham, D., Non-invasive measurements of breast tissue optical properties using frequency-domain photon migration, *Phil. Trans. R. Soc. London B*, 352, 661, 1997.
20. Sickles, E.A., Breast cancer detection with transillumination and mammography, *Am. J. Roentgenol.*, 142, 841, 1984.
21. Hoogenraad, J.H., van der Mark, M.B., Colak, S.B., Hooft, G.W., and van der Linden, E.S., First results from the Phillips Optical Mammoscope, in *Photon Propagation of Tissues III*, 31294, Benaron, D.A., Chance, B., and Ferrari, M., Eds., Plenum Press, New York, 1997, p. 184.
22. Ntziachristos, V., Ma, X.H., and Chance, B., Time-correlated single photon counting imager for simultaneous magnetic resonance and near-infrared mammography, *Rev. Sci. Instrum.*, 69, 4221, 1998.
23. Ntziachristos, V., Yodh, A.G., Schnall, M., and Chance, B., Comparison between intrinsic and extrinsic contrast for malignancy detection using NIR mammography, *Proc. SPIE*, 3597, 565, 1999.
24. Pogue, B.W., Poplack, S.D., McBride, T.O., Jiang, S., Osterberg, U.L., and Paulsen, K.D., Breast tissue and tumor hemoglobin and oxygen saturation imaging with multi-spectral near infrared computed tomography, in *Advances in Experimental Medicine and Biology Series*, Plenum Press, New York, 2001.
25. Pogue, B.W., Poplack, S.D., McBride, T.O., Jiang, S., Osterberg, U.L., and Paulsen, K.D., Near-infrared tomography: status of Dartmouth imaging studies and future directions, in progress.
26. Gopinath, S.P., Robertson, C.S., Grossman, R.G., and Chance, B., Near-infrared spectroscopic localization of intracranial hematomas, *J. Neurosurg.*, 79, 43, 1993.
27. Robertson, C.S., Gopinath, S.P., and Chance, B., A new application for near-infrared spectroscopy: detection of delayed intracranial hematomas after head injury, *J. Neurotrauma*, 12, 591, 1995.
28. Hintz, S.R., Cheong, W.F., Van Houten, J. P., Stevenson, D.K., and Benaron, D.A., Bedside imaging of intracranial hemorrhage in the neonate using light: comparison with ultrasound, computed tomography, and magnetic resonance imaging, *Pediatr. Res.*, 45, 54, 1999.
29. Hoshi, Y. and Tamura, M., Detection of dynamic changes in cerebral oxygenation coupled to neuronal function during mental work in man, *Neurosci. Lett.*, 150, 5, 1993.
30. Villringer, A., Planck, J., Hock, C., Schleinkofer, L., and Dirnagl, U., Near infrared spectroscopy (NIRS): a new tool to study hemodynamic changes during activation of brain function in human adults, *Neurosci. Lett.*, 154, 101, 1993.
31. Okada, F., Tokumitsu, Y., Hoshi, Y., and Tamura, M., Gender- and handedness-related differences of forebrain oxygenation and hemodynamics, *Brain Res.*, 601, 337, 1993.
32. Ruben, J., Wenzel, R., Obrig, H., Villringer, K., Bernarding, J., Hirth, C., Heekeren, H., Dirnagl, U., and Villringer, A., Haemoglobin oxygenation changes during visual stimulation in the occipital cortex, *Adv. Exp. Med. Biol.*, 428, 181, 1997.
33. Sakatani, K., Chen, S., Lichty, W., Zuo, H., and Wang, Y.P., Cerebral blood oxygenation changes induced by auditory stimulation in newborn infants measured by near infrared spectroscopy, *Early Hum. Dev.*, 55, 229, 1999.
34. Obrig, H., Wolf, T., Doge, C., Hulsing, J.J., Dirnagl, U., and Villringer, A., Cerebral oxygenation changes during motor and somatosensory stimulation in humans, as measured by near-infrared spectroscopy, *Adv. Exp. Med. Biol.*, 388, 219, 1996.

35. Colier, W.N., Quaresima, V., Oeseburg, B., and Ferrari, M., Human motor-cortex oxygenation changes induced by cyclic coupled movements of hand and foot, *Exp. Brain Res.*, 129, 457, 1999.
36. Kleinschmidt, A., Obrig, H., Requardt, M., Merboldt, K.D., Dirnagl, U., Villringer, A., and Frahm, J., Simultaneous recording of cerebral blood oxygenation changes during human brain activation by magnetic resonance imaging and near-infrared spectroscopy, *J. Cereb. Blood Flow Metab.*, 16, 817, 1996.
37. Hirth, C., Obrig, H., Villringer, K., Thiel, A., Bernarding, J., Muhlnickel, W., Flor, H., Dirnagl, U., and Villringer, A., Non-invasive functional mapping of the human motor cortex using near-infrared spectroscopy, *Neuroreport*, 7, 1977, 1996.
38. Sato, H., Takeuchi, T., and Sakai, K.L., Temporal cortex activation during speech recognition: an optical topography study, *Cognition*, 73, B55, 1999.
39. Hock, C., Villringer, K., Muller-Spahn, F., Wenzel, R., Heekeren, H., Schuh-Hofer, S., Hofmann, M., Minoshima, S., Schwaiger, M., Dirnagl, U., and Villringer, A., Decrease in parietal cerebral hemoglobin oxygenation during performance of a verbal fluency task in patients with Alzheimer's disease monitored by means of near-infrared spectroscopy (NIRS) — correlation with simultaneous rCBF-PET measurements, *Brain Res.*, 755, 293, 1997.
40. Hock, C., Villringer, K., Heekeren, H., Hofmann, M., Wenzel, R., Villringer, A., and Muller-Spahn, F., A role for near infrared spectroscopy in psychiatry? *Adv. Exp. Med. Biol.*, 413, 105, 1997.
41. Fallgatter, A.J. and Strik, W.K., Reduced frontal functional asymmetry in schizophrenia during a cued continuous performance test assessed with near-infrared spectroscopy, *Schizophr. Bull.*, 26, 913, 2000.
42. Bank, W. and Chance, B., Diagnosis of mitochondrial disease by NIRS, *Proc. SPIE*, 2383, 1995.
43. Bank, W. and Chance, B., An oxidative defect in metabolic myopathies: diagnosed by non-invasive tissue oximetry, *Ann. Neurol.*, 36, 830, 1994.
44. Chance, B. and Bank, W., Genetic disease of mitochondrial function evaluated by NMR and NIR spectroscopy of skeletal tissue, *Biochim. Biophys. Acta*, 1271, 7, 1995.
45. Nioka, S., Moser, D., Lech, G., Evengelisti, M., Verde, T., Chance, B., and Kuno, S., Muscle deoxygenation in aerobic and anaerobic exercise, *Adv. Exp. Med. Biol.*, 454, 63, 1998.
46. Nioka, S., Chance, B., and Nakayama, K., Possibility of monitoring mitochondrial activity in isometric exercise using NIRS, in *Oxygen Transport to Tissue*, Chance, B., Ed., Plenum Press, New York, 1998, p. 454.
47. Dougherty, T.J., Gomer, C.J., Henderson, B.W., Jori, G., Kessel, D., Korbelik, M., Moan, J., and Peng, Q., Photodynamic therapy, *J. Nat. Cancer Inst.*, 90, 889, 1998.
48. Patterson, M.S., Wilson, B.C., and Graff, R., *In vivo* tests of the concept of photodynamic threshold dose in normal rat liver photosensitized by aluminum chlorosulphonated phthalocyanine, *Photochem. Photobiol.*, 51, 343, 1990.
49. van Gemert, J.C., Berenbaum, M.C., and Gijsberg, G.H.M., Wavelength and light dose dependence in tumor phototherapy with haematoporphyrin derivative, *Br. J. Cancer*, 52, 43, 1985.
50. Farrell, T.J., Wilson, B.C., Patterson, M.S., and Olivio, M.C., Comparison of the *in vivo* photodynamic threshold dose for photofrin, mono- and tetrasulfonated aluminum phthalocyanine using a rat liver model, *Photochem. Photobiol.*, 68, 394, 1998.
51. Lilge, L., Olivo, M.C., Shatz, S.W., MaGuire, J.A., Patterson, M.S., and Wilson, B.C., The sensitivity of the normal brain and intracranially implanted VX2 tumour to intestinal photodynamic therapy, *Br. J. Cancer*, 73, 332, 1996.
52. Johnson, C.C., Optical diffusion in blood, *IEEE Trans. Biomed. Eng.*, 129, 1970.
53. Ishimaru, A., *Wave Propagation and Scattering in Random Media*, Academic Press, San Diego, 1978.
54. Furutsu, K., On the diffusion equation derived from the space-time transport equation, *J. Opt. Soc. Am. A*, 70, 360, 1980.
55. Groenhuis, R.A.J., Ferwerda, H.A., and Ten Bosch, J.J., Scattering and absorption of turbid materials determined from reflection measurements. I. Theory, *Appl. Opt.*, 22, 2456, 1983.

56. Patterson, M.S., Chance, B., and Wilson, B.C., Time resolved reflectance and transmittance for the noninvasive measurement of tissue optical properties, *Appl. Opt.*, 28, 2331, 1989.
57. Durduran, T., Chance, B., Yodh, A.G., and Boas, D.A., Does the photon diffusion coefficient depend on absorption? *J. Opt. Soc. Am. A*, 14, 3358, 1997.
58. Case, K.M. and Zweifel, P.F., *Linear Transport Theory*, Addison-Wesley, Boston, 1967.
59. Furutsu, K. and Yamada, Y., Diffusion approximation for a dissipative random medium and the applications, *Phys. Rev. E*, 50, 3634, 1994.
60. Furutsu, K., Pulse wave scattering by an absorber and integrated attenuation in the diffusion approximation, *J. Opt. Soc. Am.*, 14, 267, 1997.
61. Aronson, R. and Corngold, N., Photon diffusion coefficient in an absorbing medium, *J. Opt. Soc. Am. A*, 16, 1066, 1999.
62. Durian, D.J., The diffusion coefficient depends on absorption, *Opt. Lett.*, 23, 1502, 1998.
63. Glasstone, S. and Edlund, M.C., *The Elements of Nuclear Reactor Theory*, Van Nostrand, New York, 1952.
64. Star, W.M., Marijnissen, J.P.A., and van Gemert, M.J.C., Light dosimetry in optical phantoms and in tissues: I. Multiple flux and transport theory, *Phys. Med. Biol.*, 33, 437, 1988.
65. Davidson, B., *Neutron Transport Theory*, Clarendon, Oxford, 1957.
66. Duderstadt, J.J. and Martin, W.R., *Transport Theory*, Wiley, New York, 1979.
67. Graaff, R. and Ten Bosch, J.J., Diffusion coefficient in photon density theory, *Opt. Lett.*, 25, 43, 2000.
68. Martelli, F., Bassani, M., Alianelli, L., Zangheri, L., and Zaccanti, G., Accuracy of the diffusion equation to describe photon migration through an infinite medium: numerical and experimental investigation, *Phys. Med. Biol.*, 45, 2235, 2000.
69. Boas, D., Diffuse photon probes of structural and dynamical properties of turbid media: theory and biomedical applications, Ph.D. dissertation, University of Pennsylvania, Philadelphia, 1996.
70. Li, X., Fluorescence and diffusive wave diffraction tomographic probes in turbid media, Ph.D. dissertation, University of Pennsylvania, Philadelphia, 1998.
71. Wilson, B.C. and Patterson, M.S., The physics of photodynamic therapy, *Phys. Med. Biol.*, 31, 327, 1986.
72. Kaplan, P.D., Kao, M.H., Yodh, A.G., and Pine, D.J., Geometric constraints for the design of diffusing-wave spectroscopy experiments, *Appl. Opt.*, 32, 3828, 1993.
73. Kaplan, P.D., Optical studies of the structure and dynamics of opaque colloids, Ph.D. dissertation, University of Pennsylvania, Philadelphia, 1992.
74. Barbieri, B., Piccoli, F.D., van de Ven, M., and Gratton, E., What determines the uncertainty of phase and modulation measurements in frequency domain fluorometry? *SPIE Time Resolved Laser Spectrosc. Biochem. II*, 1204, 158, 1990.
75. Fishkin, J.B. and Gratton, E., Propagation of photon density waves in strongly scattering media containing an absorbing "semi-infinite" plane bounded by a straight edge, *J. Opt. Soc. Am. A*, 10, 127, 1993.
76. O'Leary, M.A., Boas, D.A., Chance, B., and Yodh, A.G., Refraction of diffuse photon density waves, *Phys. Rev. Lett.*, 69, 2658, 1992.
77. Boas, D.A., Oleary, M.A., Chance, B., and Yodh, A.G., Scattering and wavelength transduction of diffuse photon density waves, *Phys. Rev. E*, 47, R2999, 1993.
78. Tromberg, B.J., Svaasand, L.O., Tsay, T., and Haskell, R.C., Properties of photon density waves in multiple-scattering media, *Appl. Opt.*, 32, 607, 1993.
79. Farrell, T.J., Patterson, M.S., and Wilson, B., A diffusion theory model of spatially resolved, steady state diffuse reflectance for the noninvasive determination of tissue optical properties *in vivo*, *Med. Phys.*, 19, 879, 1992.
80. Hull, E.L., Nichols, M.G., and Foster, T.H., Quantitative broadband near-infrared spectroscopy of tissue-simulating phantoms containing erthrocytes, *Phys. Med. Biol.*, 43, 2281, 1998.
81. Solonenko, M., Cheung, R., Busch, T.M., Kachur, A., Griffin, G.M., Vulcan, T., Zhu, T.C., Wang, H.-W., Hahn, S.M., and Yodh, A.G., *In vivo* reflectance measurement of optical properties, blood oxygenation and motexafin lutetium uptake in canine large bowel, kidneys and prostates, *Phys. Med. Biol.*, 47, 1, 2002.

82. Fantini, S., Franceschini, M.A., Maier, J.S., Walker, S., and Gratton, E., Frequency domain multi-source optical spectrometer and oximeter, *Proc. SPIE*, 2326, 108, 1994.
83. Cutler, M., Transillumination of the breast, *Surg. Gynecol. Obstet.*, 48, 721, 1929.
84. Watmough, D.J., Transillumination of breast tissues: factors governing optimal imaging of lesions, *Radiology*, 147, 89, 1983.
85. Sickles, E.A., Periodic mammographic follow-up of probably benign lesions: results in 3184 consecutive cases, *Radiology*, 179, 463, 1991.
86. Wallberg, H., Alveryd, A., Bergvall, U., Nasiell, K., Sundelin, P., and Troel, S., Diaphanography in breast carcinoma, *Acta Radiol. Diagn.*, 26, 33, 1985.
87. Profio, A.E. and Navarro, G.A., Scientific basis of breast diaphanography, *Med. Phys.*, 16, 60, 1989.
88. Pera, A. and Freimanis, A.K., The choice of radiologic procedures in the diagnosis of breast disease, *Obstet. Gynecol. Clin. N. Am.*, 14, 635, 1987.
89. Homer, M.J., Breast imaging: pitfalls, controversies, and some practical thoughts, *Radiol. Clin. North Am.*, 14, 635, 1985.
90. Gisvold, J.J., Brown, L.R., Swee, R.G., Raygor, D.J., Dickerson, N., and Ranfranz, M.K., Comparison of mammography and transillumination light scanning in the detection of breast lesions, *Am. J. Roentgenol.*, 147, 191, 1986.
91. Bartrum, R.J.J. and Crow, H.C., Transillumination lightscanning to diagnose breast cancer: a feasibility study, *Am. J. Roentgenol.*, 142, 409, 1984.
92. Merrit, C.R.B., Sullivan, M.A., and Segaloff, A., Real time transillumination lightscanning of the breast, *Radiographics*, 4, 989, 1984.
93. Carlsen, E.N., Transillumination light scanning, *Diagn. Imaging*, 4, 28, 1982.
94. Marshall, V., Williams, D.C., and Smith, K.D., Diaphanography as a means of detecting breast cancer, *Radiology*, 150, 339, 1984.
95. Monsees, B., Destouet, J.M., and Totty, W.G., Light scanning versus mammography in breast cancer detection, *Radiology*, 163, 463, 1987.
96. Walker, S.A., Fantini, S., and Gratton, E., Image reconstruction by back-projection from frequency-domain optical measurements in highly scattering media, *Appl. Opt.*, 36, 170, 1997.
97. Colak, S.B., Papaioannou, D.G., 't Hooft, G.W., van der Mark, M.B., Schomberg, H., Paasschens, J.C.J., Melissen, J.B.M., and Van Asten, N.A.A.J., Tomographic image reconstruction from optical projections in light-diffusing media, *Appl. Opt.*, 36, 180, 1997.
98. Schotland, J.C., Continuous-wave diffusion imaging, *J. Opt. Soc. Am.*, 14, 275, 1997.
99. Li, X.D., Durduran, T., Yodh, A.G., Chance, B., and Pattanayak, D.N., Diffraction tomography for biochemical imaging with diffuse-photon density waves, *Opt. Lett.*, 22, 573, 1997.
100. Cheng, X. and Boas, D.A., Diffuse optical reflectance tomography with continuous-wave illumination, *Opt. Express*, 3, 118, 1998.
101. Matson, C.L. and Liu, H.L., Analysis of the forward problem with diffuse photon density waves in turbid media by use of a diffraction tomography model, *J. Opt. Soc. Am. A*, 16, 455, 1999.
102. Schotland, J.C., Haselgrove, J.C., and Leigh, J.S., Photon hitting density, *Appl. Opt.*, 32, 448, 1993.
103. O'Leary, M.A., Boas, D.A., Chance, B., and Yodh, A.G., Experimental images of heterogeneous turbid media by frequency-domain diffusing-photon tomography, *Opt. Lett.*, 20, 426, 1995.
104. Arridge, S.R., Photo-measurement density functions. Part 1: analytical forms, *Appl. Opt.*, 34, 7395, 1995.
105. Arridge, S.R. and Schweiger, M., Photon-measurement density-functions. 2. Finite-element-method calculations, *Appl. Opt.*, 34, 8026, 1995.
106. Barbour, R.L., Graber, H.L., Chang, J., Barbour, S.S., Koo, P.C., and Aronson, R., MRI-guided optical tomography: prospects and computation for a new imaging method, *IEEE Comput. Sci. Eng.*, 2, 63, 1995.
107. Yao, Y., Wang, Y., Pei, Y., Zhu, W., and Barbour, R.L., Frequency-domain optical imaging of absorption and scattering distributions using a Born iterative method, *J. Opt. Soc. Am. A*, 14, 325, 1997.

108. Paulsen, K.D. and Jiang, H., Spatially varying optical property reconstruction using a finite element diffusion equation approximation, *Med. Phys.*, 22, 691, 1995.
109. Jiang, H., Paulsen, K.D., Osterberg, U.L., Pogue, B.W., and Patterson, M.S., Optical image reconstruction using frequency-domain data: simulations and experiments, *J. Opt. Soc. Am. A*, 13, 253, 1996.
110. Paulsen, K.D. and Jiang, H., Enhanced frequency-domain optical image reconstruction in tissues through total variation minimization, *Appl. Opt.*, 35, 3447, 1996.
111. Jiang, H.B., Paulsen, K.D., Osterberg, U.L., and Patterson, M.S., Frequency-domain optical image reconstruction in turbid media: an experimental study of single-target detectability, *Appl. Opt.*, 36, 52, 1997.
112. Jiang, H., Paulsen, K.D., Osterberg, U.L., and Patterson, M.S., Improved continuous light diffusion imaging in single- and multi-target tissue-like phantoms, *Phys. Med. Biol.*, 43, 675, 1998.
113. Pogue, B.W., McBride, T.O., Prewitt, J., Osterberg, U.L., and Paulsen, K.D., Spatially variant regularization improves diffuse optical tomography, *Appl. Opt.*, 38, 2950, 1999.
114. Arridge, S.R. and Schweiger, M., A gradient-based optimisation scheme for optical tomography, *Opt. Express*, 2, 213, 1998.
115. Klibanov, M.V., Lucas, T.R., and Frank, R.M., A fast and accurate imaging algorithm in optical/diffusion tomography, *Inverse Probl.*, 13, 1341, 1997.
116. Gryazin, Y.A., Klibanov, M.V., and Lucas, T.R., Imaging the diffusion coefficient in a parabolic inverse problem in optical tomography, *Inverse Probl.*, 1, 373, 1999.
117. Eppstein, M.J., Dougherty, D.E., Troy, T.L., and Sevick-Muraca, E.M., Biomedical optical tomography using dynamic parameterization and Bayesian conditioning on photon migration measurements, *Appl. Opt.*, 38, 2138, 1999.
118. Arridge, S.R., Optical tomography in medical imaging, *Inverse Probl.*, 15, R41, 1999.
119. Zhu, Q., Durduran, T., Ntziachristos, V., Holboke, M., and Yodh, A.G., Imager that combines near-infrared diffusive light and ultrasound, *Opt. Lett.*, 24, 1050, 1999.
120. Yao, Y., Pei, Y., Wang, Y., and Barbour, R.L., A Born type iterative method for imaging of heterogeneous scattering media and its application to simulated breast tissue, *Proc. SPIE*, 2979, 232, 1997.
121. Lagendijk, A. and Biemond, J., *Iterative Identification and Restoration of Images*, Kluwer Academic, Dordrecht, the Netherlands, 1991.
122. Hansen, P.C., *Rank-Deficient and Discrete Ill-Posed Problems*, SIAM, Philadelphia, 1998.
123. Culver, J.P., Ntziachristos, V., Holboke, M.J., and Yodh, A.G., Optimization of optodearrangements for diffuse optical tomography: a singular-value analysis, *Opt. Lett.*, 26, 701, 2001.
124. Atkins, M.S., Murray, D., and Harrop, R., Use of transputers in a three-dimensional positron emission tomograph, *IEEE Trans. Med. Imaging*, 10, 276, 1991.
125. Rajan, K., Patnaik, L.M., and Ramakrishna, J., High-speed computation of the EM algorithm for PET image reconstruction, *IEEE Trans. Nucl. Sci.*, 41, 1721, 1994.
126. Chen, C.-M., An efficient four-connected parallel system for PET image reconstruction, *Parallel Comput.*, 24, 1499, 1998.
127. Gregor, J. and Huff, D.A., A computational study of the focus-of-attention EM-ML algorithm for PET reconstruction, *Parallel Comput.*, 24, 1998.
128. Zaidi, H., Labbe, C., and Morel, C., Implementation of an environment for Monte Carlo simulation of fully three-dimensional positron tomography on a high-performance parallel platform, *Parallel Comput.*, 24, 1523, 1998.
129. Miller, M.I. and Butler, C.S., Three-dimensional maximum a posteriori estimation for single photon emission computed tomography on massively-parallel computers, *IEEE Trans. Med. Imaging*, 12, 560, 1993.
130. Butler, C.S., Miller, M.I., Miller, T.R., and Wallis, J.W., Massively parallel computers for three-dimensional single-photon-emission computed tomography, *Phys. Med. Biol.*, 39, 575, 1994.
131. Chen, C.M., Lee, S.-Y., and Cho, Z.H., A parallel implementation of three-dimensional image reconstruction on hypercube multiprocessor, *IEEE Trans. Nucl. Sci.*, 37, 1333, 1990.

132. Rajan, K., Patnaik, L.M., and Ramakrishna, J., High-speed implementation of a modified PBR algorithm on DSP-based EH topology, *IEEE Trans. Nucl. Sci.*, 44, 1658, 1997.
133. Laurent, C., Peyrin, F., Chassery, J.-M., and Amiel, M., Parallel image reconstruction on MIMD computers for three-dimensional cone-beam tomography, *Parallel Comput.*, 24, 1461, 1998.
134. Woo, E.J., Hua, P., Webster, J.G., and Tompkins, W.J., A robust image reconstruction algorithm and its parallel implementation in electrical impedance tomography, *IEEE Trans. Med. Imaging*, 12, 137, 1993.
135. Joshi, S. and Miller, M., Maximum a posteriori estimation with Good's roughness for three-dimensional optical-sectioning microscopy, *J. Opt. Soc. Am.*, 10, 1078, 1993.
136. Schweiger, M., Zhukov, L., Arridge, S.R., and Johnson, C.R., Optical tomography using the SCIRun problem solving environment: preliminary results for three-dimensional geometries and parallel processing, *Opt. Express*, 4, 263, 1999.
137. Holboke, M.J., Tromberg, B.J., Li, X., Shah, N., Fishkin, J., Kidney, D., Butler, J., Chance, B., and Yodh, A.G., Three-dimensional diffuse optical mammography with ultrasound localization in a human subject, *J. Biomed. Opt.*, 5, 237, 2000.
138. Boas, D.A. and Yodh, A.G., Spatially varying dynamical properties of turbid media probed with diffusing temporal light correlation, *J. Opt. Soc. Am. A*, 14, 192, 1997.
139. Clark, N.A., Lunacek, J. H., and Benedek, G.B., A study of Brownian motion using light scattering, *Am. J. Phys.*, 38, 575, 1970.
140. Berne, P.J. and Pecora, R., *Dynamic Light Scattering*, Wiley, New York, 1976.
141. Fuller, G.G., Rallison, J.M., Schmidt, R.L., and Leal, L.G., The measurement of velocity gradients in laminar flow by homodyne light-scattering spectroscopy, *J. Fluid Mech.*, 100, 555, 1980.
142. Tong, P., Goldburg, W.I., Chan, C.K., and Sirivat, A., Turbulent transition by photon-correlation spectroscopy, *Phys. Rev. A*, 37, 2125, 1988.
143. Bertolotti, M., Crosignani, B., Di Porto, P., and Sette, D., Light scattering by particles suspended in a turbulent fluid, *J. Phys. A*, 2, 126, 1969.
144. Bourke, P.J., Butterworth, J., Drain, L.E., Egelstaff, P.A., Jakeman, E., and Pike, E.R., A study of the spatial structure of turbulent flow by intensity-fluctuation spectroscopy, *J. Phys. A*, 3, 216, 1970.
145. Tanaka, T., Riva, C., and Ben-Sira, I., Blood velocity measurements in human retinal vessels, *Science*, 186, 830, 1974.
146. Stern, M.D., *In vivo* evaluation of microcirculation by coherent light scattering, *Nature*, 254, 56, 1975.
147. Bonner, R. and Nossal, R., Model for laser Doppler measurements of blood flow in tissue, *Appl. Opt.*, 20, 2097, 1981.
148. Pine, D.J., Weitz, D.A., Chaikin, P.M., and Herbolzheimer, E., Diffusing-wave spectroscopy, *Phys. Rev. Lett.*, 60, 1134, 1988.
149. MacKintosh, F.C. and John, S., Diffusing-wave spectroscopy and multiple scattering of light in correlated random media, *Phys. Rev. B*, 40, 2382, 1989.
150. Maret, G. and Wolf, P.E., Multiple light scattering from disordered media. The effect of Brownian motion of scatterers, *Z. Phys. B*, 65, 409, 1987.
151. Pusey, P.N. and Vaughan, J.M., *Dielectric and Related Molecular Processes X XKW*, Vol. 2, Specialist Periodical Report, Davies, M., Ed., Chemical Society, London, 1975.
152. Boas, D.A., Campbell, L.E., and Yodh, A.G., Scattering and imaging with diffusing temporal field correlations, *Phys. Rev. Lett.*, 75, 1855, 1995.
153. Berne, B.J. and Pecora, R., *Dynamic Light Scattering with Applications to Chemistry, Biology, and Physics*, Krieger, Malabar, FL, 1990.
154. Brown, W., *Dynamic Light Scattering: The Method and Some Applications*, Clarendon, New York, 1993.
155. Cummings, H.Z. and Pike, E.R., *Photon Correlation and Light-Bearing Spectroscopy*, Plenum, New York, 1974.

156. Val'kov, A.Y. and Romanov, V.P., Characteristics of propagation and scattering of light in nematic liquid crystals, *Sov. Phys. JETP*, 63, 737, 1986.
157. Rice, S.O., Mathematical analysis of random noise, in *Noise and Stochastic Processes*, Wax, N., Ed., Dover, New York, 1954, p. 133.
158. Hackmeier, M., Skipetrov, S.E., Maret, G., and Maynard, R., Imaging of dynamic heterogeneities in mulitiple-scattering media, *J. Opt. Soc. Am. A*, 14, 185, 1997.
159. Benaron, D.A., Hintz, S.R., Villringer, A., Boas, D., Kleinschmidt, A., Frahm, J., Hirth, C., Obrig, H., van Houten, J.C., Kermit, E.L., Cheong, W.F., and Stevenson, D.K., Noninvasive functional imaging of human brain using light, *J. Cereb. Blood Flow Metab.*, 20, 469, 2000.
160. Danen, R.M., Wang, Y., Li, X.D., Thayer, W.S., and Yodh, A.G., Regional imager for low-resolution functional imaging of the brain with diffusing near-infrared light, *Photochem. Photobiol.*, 67, 33, 1998.
161. Villringer, A. and Chance, B., Non-invasive optical spectroscopy and imaging of human brain function, *Trends Neurosci.*, 20, 435, 1997.
162. Kelcz, F. and Santyr, G., Gadolinium-enhanced breast MRI, *Crit. Rev. Diagn. Imaging*, 36, 287, 1995.
163. Barkhof, F., Valk, J., Hommes, O.R., and Scheltens, P., Meningeal Gd-DTPA enhancement in multiple-sclerosis, *Am. J. Neuroradiol.*, 13, 397, 1992.
164. Tilcock, C., Delivery of contrast agents for magnetic resonance imaging, computed tomography, nuclear medicine and ultrasound, *Adv. Drug Delivery Rev.*, 37, 33, 1999.
165. Kedar, R.P., Cosgrove, D., McCready, V.R., Bamber, J.C., and Carter, E.R., Microbubble contrast agent for color Doppler US: effect on breast masses, *Radiology*, 198, 679, 1996.
166. Melany, M.L., Grant, E.G., Farooki, S., McElroy, D., and Kimme-Smith, C., Effect of US contrast agents on spectral velocities: *in vitro* evaluation, *Radiology*, 211, 427, 1999.
167. Thompson, S.E., Raptopoulos, V., Sheiman, R.I., McNicholas, M.M.J., and Prassopoulos, P., Abdominal helical CT: milk as a low-attenuation oral contrast agent, *Radiology*, 211, 870, 1999.
168. Jain, R., Sawhney, S., Sahni, P., Taneja, K., and Berry, M., CT portography by direct intrasplenic contrast injection: a new technique, *Abdom. Imaging*, 24, 272, 1999.
169. Knuttel, A., Schmitt, J.M., Barnes, R., and Knutson, J.R., Acousto-optic scanning and interfering photon density waves for precise localization of an absorbing (or fluorescent) body in a turbid medium, *Rev. Sci. Instrum.*, 64, 638, 1993.
170. O'Leary, M.A., Boas, D.A., Chance, B., and Yodh, A.G., Reradiation and imaging of diffuse photon density waves using fluorescent inhomogeneities, *J. Luminesc.*, 60, 789, 1994.
171. Li, X.D., Beauvoit, B., White, R., Nioka, S., Chance, B., and Yodh, A.G., Tumor localization using fluorescence of indocyanine green (ICG) in rat model, *SPIE Proc.*, 2389, 789, 1995.
172. Wu, J., Wang, Y., Perelman, L., Itzkan, I., Dasari, R.R., and Feld, M.S., Time-resolved multichannel imaging of fluorescent objects embedded in turbid media, *Opt. Lett.*, 20, 489, 1995.
173. Bambot, S.B., Lakowicz, J.R., Sipior, J., Carter, G., and Rao, G., Bioprocess and clinical monitoring using lifetime-based phase-modulation fluorometry, *Abstr. Papers Am. Chem Soc.*, 209, 11-BTEC Part 2, 1995.
174. Rumsey, W.L., Vanderkooi, J.M., and Wilson, D.F., Imaging of phosphorescence: a novel method for measuring oxygen distribution in perfused tissue, *Science*, 241, 1649, 1988.
175. Vinogradov, S.A., Lo, L.W., Jenkins, W.T., Evans, S.M., Koch, C., and Wilson, D.F., Noninvasive imaging of the distribution of oxygen in tissue *in vivo* using infrared phosphors, *Biophys. J.*, 70, 1609, 1996.
176. Lakowicz, J.R., *Principles of Fluorescence Spectroscopy*, Plenum Press, New York, 1983.
177. Mordon, S., Devoisselle, J.M., and Maunoury, *In-vivo* pH measurement and imaging of tumor-issue using a pH-sensitive fluorescent-probe (56-carboxyfluorescein) — instrumental and exper-imental studies, *Photochem. Photobiol.*, 60, 274, 1994.
178. Russell, D.A., Pottier, R.H., and Valenzeno, D.P., Continuous noninvasive measurement of *in-vivo* pH in conscious mice, *Photochem. Photobiol.*, 59, 309, 1994.
179. Sevick-Muraca, E.M. and Burch, C.L., The origin of phosphorescent and fluorescent signals in tissues, *Opt. Lett.*, 19, 1928, 1994.

180. Hutchinson, C.L., Lakowicz, J.R., and Sevick-Muraca, E.M., Fluorescence lifetime-based sensing in tissues — a computational study, *Biophys. J.*, 68, 1574, 1995.
181. Patterson, M.S. and Pogue, B.W., Mathematical-model for time-resolved and frequency-domain fluorescence spectroscopy in biological tissue, *Appl. Opt.*, 33, 1963, 1994.
182. Wu, J., Feld, M.S., and Rava, R.P., Analytical model for extracting intrinsic fluorescence in turbid media, *Appl. Opt.*, 32, 3585, 1993.
183. Hull, E.L., Nichols, M.G., and Foster, T.H., Localization of luminescent inhomogeneities in turbid media with spatially resolved measurements of CW diffuse luminescence emittance, *Appl. Opt.*, 37, 2755, 1998.
184. Feldmann, H.J., Molls, M., and Vaupel, P.W., Blood flow and oxygenation status of human tumors — clinical investigations, *Strahlenther. Onkol.*, 175, 1, 1999.
185. O'Leary, M.A., Boas, D.A., Li, X.D., Chance, B., and Yodh, A.G., Fluorescent lifetime imaging in turbid media, *Opt. Lett.*, 21, 158, 1996.
186. Li, X.D., O'Leary, M.A., Boas, D.A., Chance, B., and Yodh, A.G., Fluorescent diffuse photon density waves in homogenous and heterogeneous turbid media: analytic solutions and applications, *Appl. Opt.*, 35, 3746, 1996.
187. Li, X.D., Chance, B., and Yodh, A.G., Fluorescent heterogeneities in turbid media: limits for detection, characterization, and comparison with absorption, *Appl. Opt.*, 37, 6833, 1998.
188. Ntziachristos, V., Chance, B., and Yodh, A.G., Differential diffuse optical tomography, *Opt. Express*, 5, 230, 1999.
189. Chernomordik, V., Hattery, D.W., Grosenick, D., Wabnitz, H., Rinneberg, H., Moesta, K.T., Schlag, P.M., and Gandjbakhche, A., Quantification of optical properties of a breast tumor using random walk theory, *J. Biomed. Opt.*, 7, 80, 2002.
190. Colak, S.B., van der Mark, M.B., Hooft, G.W., Hoogenraad, J. H., van der Linden, E.S., and Kuijpers, F.A., Clinical optical tomography and NIR spectroscopy for breast cancer detection, *IEEE J. Sel. Top. Quantum Electron.*, 5, 1143, 1999.
191. McBride, T.O., Pogue, B.W., Poplack, S., Soho, S., Wells, W.A., Jiang, S., Osterberg, U.L., and Paulsen, K.D., Multispectral near-infrared tomography: a case study in compensating for water and lipid content in hemoglobin imaging of the breast, *J. Biomed. Opt.*, 7, 72, 2002.
192. Jiang, H., Iftimia, N.V., Xu, Y., Eggert, J.A., Fajardo, L.L., and Klove, K.L., Near-infrared optical imaging of the breast with model-based reconstruction, *Acad. Radiol.*, 9, 186, 2002.
193. Nioka, S., Yung, Y., Shnall, M., Zhao, S., Orel, S., Xie, C., Chance, B., and Solin, L., Optical imaging of breast tumor by means of continuous waves, *Adv. Exp. Med. Biol.*, 411, 227, 1997.
194. Pogue, B.W. and Paulsen, K.D., High-resolution near-infrared tomographic imaging simulations of the rat cranium by use of a priori magnetic resonance imaging structural information, *Opt. Lett.*, 23, 1716, 1998.
195. Siegel, A.M., Marota, J.J.A., and Boas, D.A., Design and evaluation of a continuous-wave diffuse optical tomography system, *Opt. Express*, 4, 287, 1999.
196. Hintz, S.R., Benaron, D.A., Siegel, A.M., Zourabian, A., Stevenson, D.K., and Boas, D.A., Bedside functional imaging of the premature infant brain during passive motor activation, *J. Perinat. Med.*, 29, 335, 2001.
197. Cheung, C., Culver, J.P., Takahashi, K., Greenberg, J.H., and Yodh, A.G., *In vivo* cerebrovascular measurement combining diffuse near-infrared absorption and correlation spectroscopies, *Phys. Med. Biol.*, 46, 2053, 2001.
198. Maki, A., Yamashita, Y., Ito, Y., Watanabe, E., Mayanagi, Y., and Koizumi, H., Spatial and temporal analysis of human motor activity using noninvasive NIR topography, *Med. Phys.*, 22, 1997, 1995.
199. Takahashi, K., Ogata, S., Atsumi, Y., Yamamoto, R., Shiotsuka, S., Maki, A., Yamashita, Y., Yamamoto, T., Koizumi, H., Hirasawa, H., and Igawa, M., Activation of the visual cortex imaged by 24-channel near-infrared spectroscopy, *J. Biomed. Opt.*, 5, 93, 2000.
200. Franceschini, M.A., Toronov, V., Filiaci, M., Gratton, E., and Fanini, S., On-line optical imaging of the human brain with 160-ms temporal resolution, *Opt. Express*, 6, 49, 2000.

201. Benaron, D.A. and Stevenson, D.K., Optical time-of-flight and absorbance imaging of biologic media, *Science*, 259, 1463, 1993.
202. Chance, B., Leigh, J. S., Miyake, H., Smith, D.S., Nioka, S., Greenfeld, R., Finander, M., Kaufmann, K., Levy, W., Young, M., et al., Comparison of time-resolved and unresolved measurements of deoxyhemoglobin in brain, *Proc. Natl. Acad. Sci. U.S.A*, 85, 4971, 1988.
203. Cubeddu, R., Pifferi, A., Taroni, P., Torricelli, A., and Valentini, G., Time-resolved imaging on a realistic tissue phantom: μ_s' and μ_a images versus time-integrated images, *Appl. Opt.*, 35, 4533, 1996.
204. Hebden, J. C., Arridge, S.R., and Delpy, D.T., Optical imaging in medicine: I. Experimental techniques, *Phys. Med. Biol.*, 42, 825, 1997.
205. Grosenick, D., Wabnitz, H., and Rinneberg, H., Time-resolved imaging of solid phantoms for optical mammography, *Appl. Opt.*, 36, 221, 1997.
206. Nioka, S., Luo, Q., and Chance, B., Human brain functional imaging with reflectance CWS, *Adv. Exp. Med. Biol.*, 428, 237, 1997.
207. Maki, A., Yamashita, Y., Watanabe, E., and Koizumi, H., Visualizing human motor activity by using non-invasive optical topography, *Front. Med. Biol. Eng.*, 7, 285, 1996.
208. Colier, W., van der Sluijs, M.C., Menssen, J., and Oeseburg, B., A new and highly sensitive optical brain imager with 50 Hz sample rate, *NeuroImage*, 11, 542, 2000.
209. Gratton, E., Fantini, S., Franceschini, M.A., Gratton, G., and Fabiani, M., Measurements of scattering and absorption changes in muscle and brain, *Philos. Trans. R. Soc. London B Biol. Sci.*, 352, 727, 1997.
210. Pogue, B.W., Patterson, M.S., Jiang, H., and Paulsen, K.D., Initial assessment of a simple system for frequency domain diffuse optical tomography, *Phys. Med. Biol.*, 40, 1709, 1995.
211. Chance, B., Cope, M., Gratton, E., Ramanujam, N., and Tromberg, B., Phase measurement of light absorption and scattering in human tissues, *Rev. Sci. Instrum.*, 689, 3457, 1998.
212. Fishkin, J.B., So, P.T. C., Cerussi, A.E., Fantini, S., Franceschini, M.A., and Gratton, E., A frequency-domain method for measuring spectral properties in multiply scattering media: methemoglobin absorption spectrum in a tissue-like phantom, *Appl. Opt.*, 34, 1143, 1995.
213. Quaresima, V., Colier, W.N., van der Sluijs, M., and Ferrari, M., Non-uniform quadriceps O_2 consumption revealed by near infrared multipoint measurements, *Biochem. Biophys. Res. Commun.*, 285, 1034, 2001.
214. Miura, H., McCully, K., Hong, L., Nioka, S., and Chance, B., Exercise-induced changes in oxygen status in calf muscle of ederly subjects with peripheral vascular disease using functional near infrared imaging machine, *Ther. Res.*, 2, 1585, 2000.
215. Pogue, B.W., Testorf, M., McBride, T., Osterberg, U., and Paulsen, K., Instrumentation and design of a frequency-domain diffuse optical tomography imager for breast cancer detection, *Opt. Express*, 1, 391, 1997.
216. Schmidt, F.E., Fry, M.E., Hillman, E.M.C., Hebden, J.C., and Delpy, D.T., A 32-channel time-resolved instrument for medical optical tomography, *Rev. Sci. Instrum.*, 71, 256, 2000.
217. Culver, J.P., Choe, R., Holboke, M.J., Zubkov, L., Durduran, T., Slemp, A., Ntziachristos, V., Chance, B., and Yodh, A.G., 3D diffuse optical tomography in the plane parallel transmission geometry: evaluation of a hybrid frequency domain/continuous wave clinical system for breast imaging, *Med. Phys.*, accepted.
218. Durduran, T., Choe, R., Culver, J. P., Zubkov, L., Holboke, M.J., Giammarco, J., Chance, B., and Yodh, A.G., Bulk optical properties of healthy female breast tissue, *Phys. Med. Biol.*, 47, 2847, 2002.
219. Yang, Y., Liu, H., Li, X., and Chance, B., Low-cost frequency-domain photon migration instrument for tissue spectroscopy, oximetry and imaging, *Opt. Eng.*, 36, 1562, 1997.
220. Flock, S.T., Jacques, S.L., Wilson, B.C., Star, W.M., and van Gemert, M.J.C., Optical properties of Intralipid: a phantom medium for light propagation studies, *Lasers Surg. Med.*, 12, 510, 1992.
221. van Staveren, H.J., Moes, C.J.M., van Marle, J., Prahl, S.A., and van Gemert, M.J.C., Light scattering in Intralipid — 10% in the wavelength range of 400 to 1100 nm, *Appl. Opt.*, 30, 4507, 1991.

222. Gros, C., Quenneville, Y., and Hummel, Y., Breast diaphanology, *J. Radiol. Electrol. Med. Nucl.*, 53, 297, 1972.
223. Alveryd, A., Andersson, I., Aspegren, K., Balldin, G., Bjurstam, N., Edstrom, G., Fagerberg, G., Glas, U., Jarlman, O., Larsson, S.A., et al., Lightscanning versus mammography for the detection of breast cancer in screening and clinical practice. A Swedish multicenter study, *Cancer*, 65, 1671, 1990.
224. Shah, N., Cerussi, A., Eker, C., Espinoza, J., Butler, J., Fishkin, J., Hornung, R., and Tromberg, B., Noninvasive functional optical spectroscopy of human breast tissue, *Proc. Natl. Acad. Sci. U.S.A.*, 98, 4420, 2001.
225. Sevick-Muraca, E.M., Reynolds, J. S., Troy, T.L., Lopez, G., and Paithankar, D.Y., Fluorescence lifetime spectroscopic imaging with measurements of photon migration, *Ann. N.Y. Acad. Sci.*, 838, 46, 1998.
226. Hawrysz, D.J. and Sevick-Muraca, E.M., Developments toward diagnostic breast cancer imaging using near-infrared optical measurements and fluorescent contrast agents, *Neoplasia*, 2, 388, 2000.
227. Tromberg, B.J., Shah, N., Lanning, R., Cerussi, A., Espinoza, J., Pham, T., Svaasand, L., and Butler, J., Non-invasive *in vivo* characterization of breast tumors using photon migration spectroscopy, *Neoplasia*, 2, 26, 2000.
228. Ntziachristos, V., Ma, X.H., Yodh, A.G., and Chance, B., Multichannel photon counting instrument for spatially resolved near infrared spectroscopy, *Rev. Sci. Instrum.*, 70, 193, 1999.
229. Benaron, D.A., Hintz, S.R., Villringer, A., Boas, D., Kleinschmidt, A., Frahm, J., Hirth, C., Obrig, H., van Houten, J.C., Kermit, E.L., Cheong, W.F., and Stevenson, D.K., Noninvasive functional imaging of human brain using light, *J. Cereb. Blood Flow Metab.*, 20, 469, 2000.
230. Boas, D.A., Meglinsky, I.V., Zemany, L., Campbell, L.E., Chance, B., and Yodh, A.G., Diffusion of temporal field correlation with selected applications, *Proc. SPIE*, 2732, 34, 1996.
231. Briers, J.D., Laser Doppler and time-varying speckle: a reconciliation, *J. Opt. Soc. Am. A*, 13, 345, 1996.
232. Dunn, A.K., Bolay, H., Moskowitz, M.A., and Boas, D.A., Dynamic imaging of cerebral blood flow using laser speckle, *J. Cereb. Blood Flow Metab.*, 21, 195, 2001.
233. Kuebler, W.M., Sckell, A., Habler, O., Kleen, M., Kuhnle, G.E.H., Welte, M., Messmer, K., and Goetz, A.E., Noninvasive measurement of regional cerebral blood flow by near-infrared spectroscopy and indocyanine green, *J. Cereb. Blood Flow Metab.*, 18, 445, 1998.
234. Patel, J., Marks, K., Roberts, I., Azzopardi, D., and Edwards, A.D., Measurement of cerebral blood flow in newborn infants using near infrared spectroscopy with indocyanine green, *Pediatr. Res.*, 43, 34, 1998.
235. Gopinath, S.P., Robertson, C.S., Contant, C.F., Narayan, R.K., Grossman, R.G., and Chance, B., Early detection of delayed traumatic intracranial hematomas using near-infrared spectroscopy, *J. Neurosurg.*, 83, 438, 1995.
236. Ogawa, S., Tank, D., Menon, R., Ellermann, J., Kim, S.-G., Merkel, H., and Ugurbil, K., Intrinsic signal changes accompanying sensory stimulation: functional brain mapping with magnetic resonance imaging, *Proc. Natl. Acad. Sci. U.S.A.*, 89, 5951, 1992.
237. Kwong, K.K., Belliveau, J.W., Chesler, D.A., Goldberg, I.E., Weisskoff, R.M., Poncelet, B.P., Kennedy, D.N., Hoppel, B.E., Cohen, M.S., Turner, R., Cheng, H.-M., Brady, T.J., and Rosen, B.R., Dynamic magnetic resonance imaging of human brain activity during primary sensory stimulation, *Proc. Natl. Acad. Sci. U.S.A.*, 89, 5675, 1992.
238. Jobsis, F.F., Nonivasive, infrared monitoring of cerebral and myocardial oxygen sufficiency and circulatory parameters, *Science*, 198, 1264, 1977.
239. Wyatt, J.S., Cope, M., Delpy, D.T., Wray, S., and Reynolds, E.O.R., Quantification of cerebral oxygenation and haemodynamics in sick newborn infants by near infrared spectrophotometry, *Lancet*, ii, 1063, 1986.
240. Chance, B. and Williams, G.R., The respiratory chain and oxidative phosphorylation, *Adv. Enzymol.*, 17, 65, 1956.

241. Lockwood, A.H., LaManna, J.C., Snyder, S., and Rosenthal, M., Effects of acetazolamide and electrical stimulation on cerebral oxidative metabolism as indicated by cytochrome oxidase redox state, *Brain Res.*, 308, 9, 1984.
242. Wong Riley, M.T., Cytochrome oxidase: an endogenous metabolic marker for neuronal activity, *Trends Neurosci.*, 12, 94, 1989.
243. Kohl, M., Nolte, C., Heekeren, H.R., Horst, S., Scholz, U., Obrig, H., and Villringer, A., Changes in cytochrome-oxidase oxidation in the occipital cortex during visual stimulation: improvement in sensitivity by the determination of the wavelength dependence of the differential pathlength factor, *Proc. SPIE*, 3194, 18, 1998.
244. Wobst, P., Wenzel, R., Kohl, M., Obrig, H., and Villringer, A., Linear aspects of changes in deoxygenated hemoglobin concentration and cytochrome oxidase oxidation during brain activation, *Neuroimage*, 13, 520, 2001.
245. Gratton, E., Fantini, S., Franceschini, M.A., Gratton, G., and Fabiani, M., Measurements of scattering and absorption changes in muscle and brain, *Philos. Trans. R. Soc. London B Biol. Sci.*, 352, 727, 1997.
246. Steinbrink, J., Kohl, M., Obrig, H., Curio, G., Syre, F., Thomas, F., Wabnitz, H., Rinneberg, H., and Villringer, A., Somatosensory evoked fast optical intensity changes detected non-invasively in the adult human head, *Neurosci. Lett.*, 291, 105, 2000.
247. Stepnoski, R.A., LaPorta, A., Raccuia-Behling, F., Blonder, G.E., Slusher, R.E., and Kleinfeld, D., Noninvasive detection of changes in membrane potential in cultured neurons by light scattering, *Proc. Natl. Acad. Sci. U.S.A.*, 88, 9382, 1991.
248. Cheung, C., Culver, J. P., Takahashi, K., Greenberg, J.H., and Yodh, A.G., *In vivo* cerebrovascular measurement combining diffuse near-infrared absorption and correlation spectroscopies, *Phys. Med. Biol.*, 46, 2053, 2001.
249. Mayhew, J., Johnston, D., Martindale, J., Jones, M., Berwick, J., and Zheng, Y., Increased oxygen consumption following activation of brain: theoretical footnotes using spectroscopic data from barrel cortex, *Neuroimage*, 13, 975, 2001.
250. Mayhew, J., Zheng, Y., Hou, Y., Vuksanovic, B., Berwick, J., Askew, S., and Coffey, P., Spectroscopic analysis of changes in remitted illumination: the response to increased neural activity in brain, *Neuroimage*, 10, 304, 1999.
251. Simoes, C.H.R., Relationship between responses to contra- and ipsilateral stimuli in the human second somatosensory cortex SII, *Neuroimage*, 10, 408, 1999.
252. Spiegel, J.T.J., Gawehn, J., Stoeter, P., and Treede, R.D., Functional MRI of human primary somatosensory and motor cortex during median nerve stimulation., *Clin. Neurophysiol.*, 110, 47, 1999.
253. Allison, J.D.M.K., Loring, D.W., Figueroa, R.E., and Wright, J.C., Functional MRI cerebral activation and deactivation during finger movement, *Neurology*, 54, 135, 2000.
254. Boas, D.A., O'Leary, M.A., Chance, B., and Yodh, A.G., Detection and characterization of optical inhomogeneities with diffuse photon density waves: a signal-to-noise analysis, *Appl. Opt.*, 36, 75, 1997.
255. Matson, C.L., Deconvolution-based spatial resolution in optical diffusion tomography, *Appl. Opt.*, 40, 5791, 2001.
256. Moon, J.A. and Reintjes, J., Image resolution by use of multiply scattered light, *Opt. Lett.*, 19, 521, 1994.
257. Moon, J.A., Mahon, R., Duncan, M.D., and Reintjes, J., Resolution limits for imaging through turbid media with diffuse light, *Opt. Lett.*, 1591, 1993.
258. Pogue, B.W. and Paulsen, K.D., High-resolution near-infrared tomographic imaging simulations of the rat cranium by use of a priori magnetic resonance imaging structural information, *Opt. Lett.*, 23, 1716, 1998.
259. Zhu, Q., Conant, E., and Chance, B., Optical imaging as an adjunct to sonograph in differentiating benign from malignant breast lesions, *J. Biomed. Opt.*, 5, 229, 2000.

260. Barbour, R.L., Graber, H.L., Chang, J., Barbour, S.S., Koo, P.C., and Aronson, R., MRI-guided optical tomography: prospects and computation for a new imaging method, *IEEE Comput. Sci. Eng.*, 2, 63, 1995.
261. Ntziachristos, V., Yodh, A.G., Schnall, M., and Chance, B., MRI-guided diffuse optical spectroscopy of malignant and benign breast lesions, *Neoplasia*, 4, 347, 2002.
262. Arridge, S.R., Schweiger, M., Hiraoka, M., and Delpy, D.T., Performance of an iterative reconstruction algorithm for near infrared absorption and scatter imaging, *Proc. SPIE*, 1888, 360, 1993.
263. Schweiger, M., Arridge, S.R., and Delpy, D.T., Application of the finite-element method for the forward and inverse models in optical tomography, *J. Math. Imaging Vision*, 3, 263, 1993.
264. Arridge, S.R. and Schweiger, M., Inverse methods for optical tomography, in *Information Processing in Medical Imaging (IPMI'93 Proceedings)*, Lecture Notes in Computer Science, 687, Springer-Verlag, Berlin, 1993, p. 259.
265. Boas, D.A., Gaudette, T.J., and Arridge, S.R., Simultaneous imaging and optode calibration with diffuse optical tomography, *Opt. Express*, 8, 263, 2001.

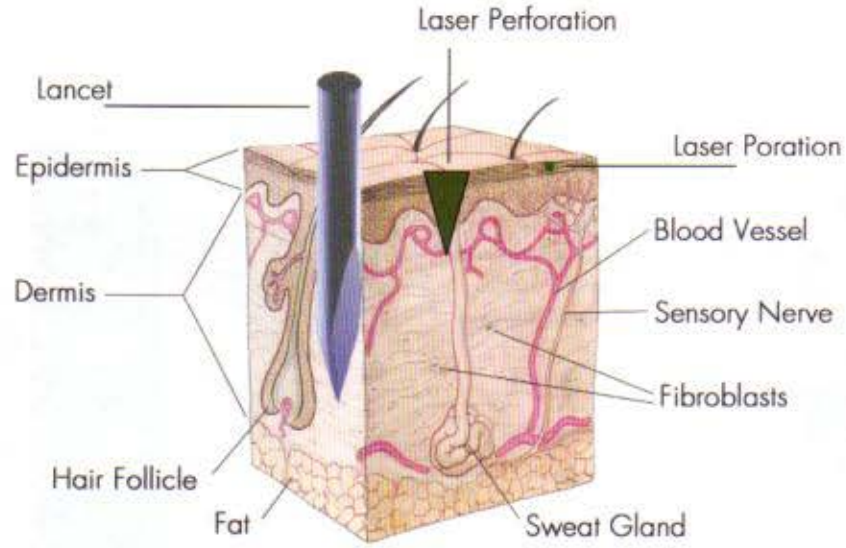

COLOR FIGURE 18.6 Cross section of skin comparing the depth of penetration incurred for a standard lancet to that of both the laser performation and laser poration approaches.

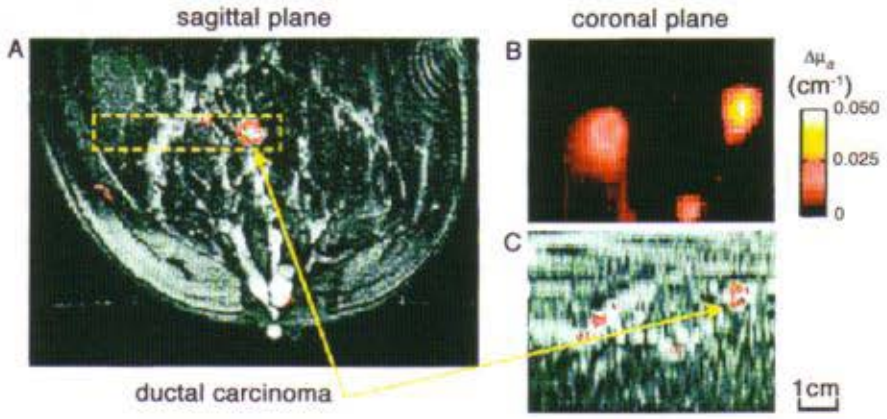

COLOR FIGURE 21.14 A dynamic MRI and contrast-enhanced DOT image of a ductal carcinoma. (A) A dynamic sagittal MR image after Gd contrast enhancement passing through the center of the malignant lesion. (B) The coronal DOT image, perpendicular to the plane of the MRI image in (A), but in the volume of interest indicated in (A) by the dashed-line box. (C) The dynamic MR coronal image resliced from the same volume of interest and same dimensions as (B).